

École polytechnique de Louvain

Design of an ultra-low-power energy-harvesting audio sensor for ecosystem monitoring

Author: **Martin BRAQUET^a**
Supervisors: **David BOL, Ramin SADRE**
Readers: **Rémi DEKIMPE, Denis FLANDRE**
Academic year 2019–2020
Master [120] in Electro-mechanical Engineering

^amartin.braquet@hotmail.com

Abstract

The Internet of Things (IoT) is predicted to lead to the deployment of a very large number (possibly trillions) of connected smart sensors for various applications. Such a massive deployment of smart sensors is not environmentally sustainable if the smart sensors are replaced every two years because of the pressure they put on natural resources and the ecotoxicity of the e-waste they generate.

Furthermore, the rising climate change due to ecosystem destruction involves monitoring forests in order to analyze and preserve the ecosystem. Such monitoring is typically achieved manually via a person who samples data less than once a day, which fails to provide strong results and asks for human presence during data acquisition.

To solve these issues, the focus of this master thesis is on the development of an autonomous and efficient audio smart sensor continuously analyzing the forest ecosystem. To fulfill the energy constraints implied by its total autonomy, this sensor harvests energy from the environment through miniaturized photovoltaic cells sized according to the sun illuminance throughout days and seasons, using an environmentally-friendly and non-toxic supercapacitor to store energy. With a 15+ year lifetime, this fully autonomous device operates at an optimized 2.5 V supply voltage reaching 22.1 mW of average power harvesting/consumption. An electret condenser microphone collects a signal as low as 16 dB_{SPL} (compared to a 14.22 dB_{SPL} input-referred noise), which is then amplified in the full frequency range of bird emission (20 Hz – 20 kHz) by a low-noise and low-power analog front-end. This signal is further processed in an ultra-low-power chip embedding a microcontroller, alternating between run and sleep modes with a 1/3 duty cycle, and a transceiver optimized for IoT applications with LoRaWAN networks.

The microcontroller detects sounds when birds are active (typically during the day for more than 12 hours) and ensures the radio-frequency communication at night depending on the supercapacitor voltage that is carefully monitored in real time. It sends information about the bird species encountered during the day, as well as their apparition frequency. In case of firmware update, this device receives the associated fragments when its energy is sufficient and it automatically changes the firmware with energy-optimized software requiring only 10.6 J for the whole update.

By computing the weighted average frequency of the received sounds, the smart sensor is able to discriminate between four common birds in Belgium: the pigeon, blackbird, great tit and blue tit. For each species, several songs have been analyzed and used to train a k -nearest neighbors (KNN) classifier working in the real-time embedded system. Its precision, defined as the likelihood to find the correct species, reaches 94% for songs coming from the previously learned database. For newly analyzed sounds, the detection algorithm performs likewise. More complex machine-learning algorithms could finally be further designed to discriminate between more species.

Acknowledgements

This thesis has been written throughout my last year at UCLouvain. It gave me the opportunity to have a first glimpse into an important work required for the procurement of a master's degree in engineering. During this substantial work, I would like to thank the following people, starting with the most meaningful ones, for their important hints and source of motivation.

First of all, I would like to thank my main supervisor, Prof. D. Bol, for his precious advice. In his works, I deeply appreciated his way to approach a problem, starting with a technological/ecological/social need and then solving it by considering all the factors in the process (systemic approach). His maturity, sensibility and motivation to handle such problems made one of the most important marks on me throughout my studies at UCLouvain.

Second, I would like to thank Tim Hess who wrote his thesis on a same topic but more focused on the wireless communication. We have had great collaborations to produce the final model of this work. He gave me important advice for the overall design and soldering of the PCB, more specifically on the handling of KiCad (a PCB design tool).

Third, I would like to thank the members of the ECS group⁰ and more specifically Rémi Dekimpe for his constant supervision through the year. He proved his availability at any time and had precious hints.

I would also like to thank my second supervisor, Prof. R. Sadre, for his availability. Likewise, I want to thank Prof. D. Flandre in advance for the reading of this thesis, as well as for his engaging courses given during my curriculum. More generally, I need to thank all the people who contributed to this work, e.g. for accessing the electronics lab and the ordering of the required materials.

⁰Electrical Circuits and Systems group led by Professors D. Bol and D. Flandre at UCLouvain.

Contents

1	Introduction	6
2	Use case	9
2.1	State of the art of IoT sensors for forest monitoring	9
2.2	General architecture	10
2.3	Requirements analysis	11
3	Energy storage	13
3.1	Primary batteries	14
3.2	Secondary batteries	15
3.3	Supercapacitors	16
3.4	New developments	16
3.5	Shape	17
3.6	Comparison	17
3.7	Selection	19
4	Power management	20
4.1	Operating voltage design	20
4.2	Power management unit	20
5	Sensing subsystem	25
5.1	Microphone	27
5.2	Analog front-end	32
6	Data processing and transceiver	43
6.1	Microcontroller	43
6.2	Transceiver	44
7	Power supply	46
7.1	Power consumption	46
7.2	Solar cells	49
7.3	Supercapacitor sizing	56
8	Final model	59
8.1	Description	59
8.2	Design	59
8.3	Validation	60

9 Inference algorithm	65
9.1 Peak frequency extraction	65
9.2 Spectrogram decomposition	66
10 Improvement perspectives	72
10.1 Power management	72
10.2 Refinement of inference algorithms	72
10.3 Robustness under difficult conditions	73
11 Conclusion	74
A Transimpedance amplifier	76
B Noise gain of the microphone amplifier	77
C PCB layout and schematic	78

List of Figures

2.1	Block diagram of a general IoT sensor node	11
3.1	Ragone plot showing specific energy versus specific power for various energy-storing devices	13
4.1	AEM10941 simplified schematic view	21
4.2	Boost conversion efficiency (solar cells – supercap) of the AEM10941	22
4.3	High-voltage LDO regulation at 2.5 V in function of the load current	23
4.4	High-voltage LDO efficiency at 2.5 V in function of the load current	24
5.1	General sound wave description	25
5.2	A-weighting curve	26
5.3	Block diagram of the sensing subsystem	27
5.4	IV curve of several microphones	31
5.5	Microphone and analog front-end circuit	32
5.6	Resolution and RMS values of ADC voltage	34
5.7	Range of p , V_{mic} and V_{ADC} along the dB scale	36
5.8	Comparison of input-referred noise and current consumption for several operational amplifiers	39
5.9	Voltage noise and resolution at the amplification output	39
5.10	Noise voltage spectral density from AFE at the amplification output (from LTSPICE)	40
5.11	AC transfer function of the amplification circuit (from LTSPICE)	42
7.1	Current consumption of the CMWX1ZZABZ without TX/RX	47
7.2	Current consumption for sending one packet of 51 bytes	48
7.3	Current consumption for a FUOTA	48
7.4	IV and PV curves of a typical solar cell: SM141K06L	50
7.5	Daily luminosity (Louvain-la-Neuve, from March 3 to March 6, 2020)	51
7.6	Sunlight towards Earth at the equinox	52
7.7	Daily view of the harvested power with SM141K06L solar cells	52
7.8	Input power and output current for six solar cells and a typical profile of cyclic consumption	53
7.9	Voltage across the supercapacitor for three numbers of cells	55
7.10	Voltage across the supercapacitor for three different capacitances	56
7.11	Constant current charge and discharge: 90 F / 5.6 V	57
7.12	Voltage split for a 90 F / 4.2 V supercap coupled with the AEM10941	58
8.1	Electronics diagram of the final model	59

8.2	Pictures of the final model	60
8.3	Supercapacitor discharge under a constant current of 500 mA	62
8.4	Analysis of a pure sine wave at 1 kHz	63
8.5	Noise at the ADC input	63
9.1	Peak frequencies associated with a great tit song	66
9.2	Spectrograms of two sounds from the blue tit computed with this sensor node	67
9.3	Spectrograms of four different bird songs computed with this sensor node	68
9.4	Precise spectrogram of the great tit song (from a bird song database)	69
9.5	Repartition of the weighted average frequency among the species learning samples	70
9.6	Predictions on new samples with the sensor node	71
A.1	Simplified transimpedance amplification circuit	76
B.1	Simplified transimpedance amplification circuit for the noise gain	77
C.1	PCB layout	78
C.2	PCB schematics	79

List of Tables

3.1	Comparison of various types of energy storage	18
4.1	Characteristics of the AEM10941 PMU	21
4.2	Values of maximum efficiency for the src – boost conversion with a 10 mA input current	23
5.1	Typical sound pressure levels	26
5.2	Sound wave characteristics at the sensor	27
5.3	Comparison of several types of microphone	30
5.4	Comparison of several electret condenser microphones	31
5.5	Operating point of the AOM-5024L-HD-R microphone	32
5.6	Characteristics of the selected microphone: AOM-5024L-HD-R	33
5.7	Characteristics of the selected operational amplifier: OPA2834	39
5.8	Final values for the amplification circuit	42
7.1	Description of the theoretical power consumption in the system	49
7.2	Comparison of several solar cells	50
7.3	Comparison of several supercapacitors	57
8.1	Description of the current consumption in the system	60
8.2	Harvested power from the solar cells in function of the MMP ratio	61
8.3	Harvested current under different lighting from the solar cells at the MMP voltage	61
9.1	Processing time for one spectrogram data chunk with 128 samples	67
9.2	Number of right predictions on the learning samples with the sensor node	71
11.1	SWOT analysis of this smart sensor	75

Chapter 1

Introduction

This thesis is dedicated to people interested in audio monitoring and its subsequent recent rise, as well as in the technical details/constraints related to the design of such sensors. It is accessible for people from diverse domains, but a background in engineering is nonetheless advised.

Context

The Internet of Things (IoT) is a system of interrelated computing devices that are provided with unique identifiers and the ability to transfer data over a network without requiring human-to-human or human-to-computer interaction. It is predicted to lead to the deployment of a very large number (possibly trillions) of connected smart sensors for various applications. However, such a massive deployment of smart sensors is not environmentally sustainable if the smart sensors are replaced every two years because of the pressure they put on natural resources and the ecotoxicity of the e-waste they generate. Therefore, it is needed to fight obsolescence in the IoT domain by enabling a 10+ year lifetime for the smart sensors.

Audio monitoring Forests are important sources for biodiversity and ecological balance. They provide many benefits and it is the main function for water and soil conservation, genetic resources for plant and animal, and also a source of wood supply and other forest goods. They also have important benefits on human physical and mental health [1]. However, recently the green forest environment has been interrupted by unethical activities such as development activities that decrease the benefits of the forest contribution. Thus, in order to ensure long-term forest autonomy, it is important to implement a monitoring system that is responsible for providing effective monitoring for forest environment. Forest monitoring is not limited to environmental issues only, but it also includes fire monitoring and detection in forests [2]. To set the problems, a policy-relevant infrastructure for monitoring of forest ecosystems has been recently proposed in the European Union [3].

Nowadays, some key variables, such as tree health and biodiversity, are only collected once a year because they must be assessed by a well-trained human operator. This low observation frequency considerably limits the possibility of characterizing evolution trends relating them with explanatory causes.

To achieve this goal of an autonomous long-lasting sensor, energy needs to be harvested from the environment through miniaturized photovoltaic cells, using batteries whose chemistry does not wear out and having reconfiguration capabilities to keep up with application, security and communication protocol updates.

Contributions

In this master thesis, a operational device is built to monitor bird songs in forest. It is attached to a tree, it records sounds, analyzes and sends them wirelessly. Thanks to a supercapacitor and solar cells, it is fully autonomous, efficient and connected to the cloud. It is in operation for more than 15 years without any human assistance and can discriminate between bird songs which are rather distinct (based on their frequency spectrum).

The objectives of this thesis are multiple. It first aims at improving the audio monitoring quality in forest while reducing human interactions, especially in areas with difficult access. Via this text, it also includes providing useful information for diverse people interested in the domain, such as companies willing to improve ecosystem monitoring or students facing a related problem.

For this purpose, all the files used for the simulations as well as the LaTeX source code of this thesis are fully open-source under the *MIT* license¹ at <https://github.com/MartinBraquet/master-thesis-UCLouvain>.

Structure

The structure of this thesis has been carefully built to replicate the design process of this sensor. Indeed, the chapters totally mimic the real chronology throughout the year, in such a way that each chapter is mainly based on the design choices of the previous chapters.

Chapter 2 describes the use case, by detailing the state-of-the-art of audio monitoring, the requirements for the system and its general architecture.

Chapter 3 details the different types of energy storage, from the primary battery to the supercapacitor and the new developments. They are then compared and the most suited for this application is selected.

Chapter 4 is dedicated to the power management. The selection of the supply voltage as well as the operation of the power management unit are explained.

Chapter 5 analyzes the sensing subsystem. After a brief review of the principles of wave propagation, different kinds of microphones are detailed and compared, leading to the selection of the most meaningful. Then, the analog front-end is detailed, associated with the design of each component. The best microphone is then chosen such that it optimizes the noise / power consumption specifications.

Chapter 6 gives a description of the data processing and transmission, with an emphasis on the microcontroller behavior.

¹Provided that the reader gives appropriate credit, he is free to copy and redistribute the material in any medium or format under the same license as the original. He has permission to remix, transform, and build upon the material for any purpose, even commercially.

Chapter 7 describes the power supply by first summarizing the whole power consumption. The best solar cells are then selected in accordance with the expected sun illuminance. The supercapacitor is characterized and its capacitance is designed according to the power management unit specifications.

Chapter 8 details the final model, with its design and prototyping, and ends with a complete validation of the system.

Chapter 9 provides different inference algorithms used to process, inside the microcontroller, the received data from the microphone. Experimental results are provided and reviewed.

Chapter 10 gives some perspectives of improvement for an application which is still new with great perspectives.

Chapter 11 ends this work with a conclusion. The appendices give additional details on the transimpedance amplifier, the noise gain of the microphone amplifier and the PCB layout/schematic of the final model.

Chapter 2

Use case

This chapter describes a few state-of-the-art IoT smart sensors for forest monitoring and the process/systems required to accomplish the aforementioned goals.

2.1 State of the art of IoT sensors for forest monitoring

Since 2000, *wireless sensor networks* (WSNs) have received increasing attention in research on automatic natural environments [4].

For forest monitoring, research has already been achieved as attested by the following state of the art. First, in [5], they worked on autonomous recording units which have been widely used in a large number of bird studies in recent years, but challenges remain in estimating abundance based on acoustic monitoring. They tested whether vocal activity rate index (VAR; the number of songs per unit time for a species), recorded using autonomous recording units, was related to population abundance in two terrestrial bird species. Second, in [6], they illustrate a forest monitoring system solution of wireless sensor networks based on ZigBee by using sensor nodes and coordinator nodes. Third, in [7], a 20-day wireless sensor network of 18 nodes has been deployed in a mountain area. It has a good fidelity since they received 87% of sent sample data. Their primary concern remains to enlarge the network scale and prolong the network lifetime.

However, these previous works show that the use of WSNs has been limited to simple tasks due to key technological issues. First, the high power consumption of the sensor nodes in operation leads to a trade-off between the density of the sensor deployment (limited by the frequency of battery replacement by an operator) and the complexity of the ecosystem parameters to monitor. Second, the limited range of low-power wireless communication prevented large-scale deployment. Third, the monitoring of complex, non-directly observable parameters (e.g. bird population, tree health) is impeded by the lack of low-power algorithms (typically machine learning) that would process on-chip data. However, today, technological advances in ultra-low-power processors [8], IoT communications and artificial intelligence open new possibilities. A brief insight of them will be described in this work.

Communication In regard to these topics, low power communication protocols also appeared. There is a trade-off between energy and range that such devices can sustain. The data rate, i.e.

the amount of data transmitted per unit of time, can be tuned as a degree of freedom to adjust this trade-off. It is thus desirable to produce reconfigurable solutions.

For long-range communications, a low-power wide-area network (LPWAN) such as LoRa is used. LoRa is a spread spectrum modulation technique derived from chirp spread spectrum (CSS) technology and is the first low-cost implementation of chirp spread spectrum for commercial usage. LoRa also has a lot of applications in urban areas, such as waste management in smart cities [9].

For short-range communications, a wireless personal area network (WPAN) such as Bluetooth low energy (BLE) is used since they consume less energy per bit sent ($30\text{ nJ}/\text{bit}$ compared to $1\text{ }\mu\text{J}/\text{bit}$ for LoRa [10]). For this, multiple challenges exist such as spectrum congestion (due to the limited data rate), data deluge, security flaws, natural resources, ecotoxicity, battery charging/replacement. Multi-hop transfer describes communications between several sensors, they can help solve some of these issues by increasing the range but with a costly synchronization [11].

Data processing With the limited data rate of low-power communication protocols, local data storage and processing are required to extract and store meaningful information.

In addition to on-chip data processing, edge computing has been proposed to further reduce the data flow and hence the power consumption, it refers to the enabling technologies allowing computation to be performed at the edge of the network, on downstream data on behalf of cloud services and on upstream data on behalf of IoT services [12]. Here, edges are any computing and network resources along the path between data sources and cloud data center (e.g. for forest monitoring, a gateway between the smart sensors and the cloud data centers).

For sound analysis, some algorithms such as Blind Audio Source Separation (BASS) have been developed to discriminate the sound from several sources (e.g. birds) with the help of several sensors (that is, microphones). Methods exist to rank existing BASS algorithms according to their performance on the same test data [13].

2.2 General architecture

The general architecture of this type of sensor node is given in Figure 2.1. A sensor is a device which probes, processes and sends diverse physical subjects in an environment. For this work, the physical subject is the sound pressure.

Inside the sensor node, there are typically four submodules:

- *Sensor*: The sensor captures data from its environment by producing a measurable response to a change in a physical condition like temperature or pressure. It has specific characteristics such as accuracy, sensitivity... The physical signal is typically filtered and amplified in an analog front-end (AFE). The continual analog signal is then sent to a controller for further processing, either in continuous form or in digital form via an analog-to-digital converter (ADC).
- *Controller*: The data are processed in a controller, which is most often a microcontroller for its flexibility to connect to other devices, ease of programming, low cost and low

power consumption. The microcontroller performs tasks, processes data and controls the functionality of other components in the sensor node.

- *Transceiver*: The transmission (TX) and reception (RX) are combined in a transceiver which allows exchanging data, mostly wirelessly through radio frequency (RF) with an antenna. WSNs tend to use license-free communication frequencies¹, LoRa uses for example license-free sub-gigahertz radio frequency bands (like 433 MHz, 868 MHz (Europe)) enabling long-range transmissions with low power consumption.
- *Power management*: Since the wireless sensor node is often placed in a hard-to-reach location, changing the battery regularly can be costly and inconvenient. Hence, an important aspect in the development of a wireless sensor node is ensuring that there is always adequate energy available to power the system. The sensor node consumes power for sensing, data processing and communicating. Power is stored either in batteries or capacitors. They renew their energy from solar sources, radio frequency, temperature differences, or vibration.

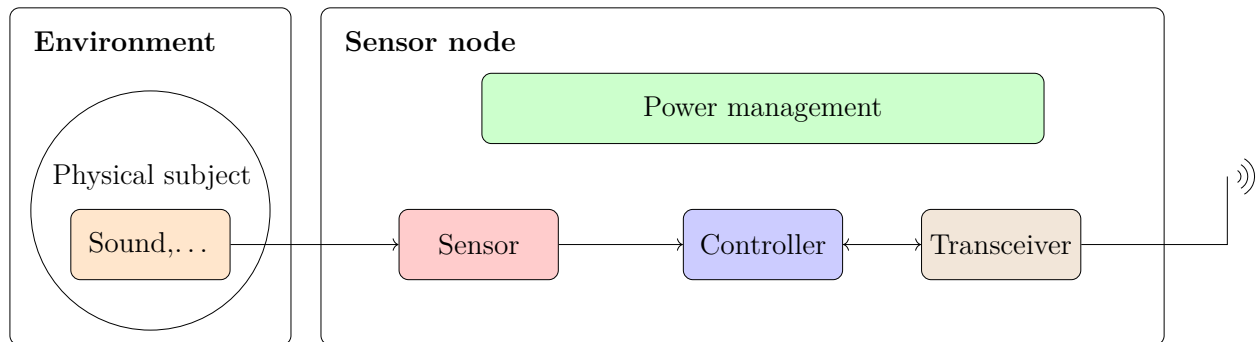


Figure 2.1: Block diagram of a general IoT sensor node

Because energy is the most important scarcity in such sensors (defining its lifetime), one has to keep in mind the power consumption of each block throughout the design. It is expected that the parts with the most power consumption are the microcontroller, the transceiver and the microphone. The other parts will be designed to be negligible compared to the formers.

2.3 Requirements analysis

The sensor that will be produced needs to fit the following requirements:

- The microphone detects sounds up to 50 m in order to produce a reasonable inventory of bird population.
- It is able to communicate wirelessly by receiving and transmitting data under power constraints.
- Based on the continuously received sound, the sensor has to discriminate the bird species among a small group (4) of selected birds.

¹The ISM radio bands are portions of the radio spectrum reserved internationally for industrial, scientific and medical (ISM) purposes other than telecommunications.

- The lifetime is one of the most important demands for this application, the sensor has to work fully autonomously (day and night) for at least 15 years.
- The materials used for the design, particularly the energy storage element, must have low toxicity.
- The device cannot be invasive and should be easy to install. The total volume must not exceed 200 mm × 200 mm × 55 mm to respect the forest ecosystem and be easily placed on a tree. The main part of the volume will be due to the storage element and the solar cells.
- For a massive deployment, the cost cannot exceed 15 euros.

Chapter 3

Energy storage

Energy storage has an important role in sensor applications. First, this role can be identified as either a unique power for the application, or as a temporary storage of energy provided by the energy harvester. In the framework of this thesis, the latter is considered since solar cells (energy harvester) will bring energy to the system, which is stored in an energy storage element.

Then, one has to characterize the main figures of merits such as the energy density, the maximum self-discharge and application conditions, as well as financial and environmental considerations.

A Ragone plot is typically used for comparing the energy density of various energy-storing devices. On such a chart, the values of specific energy density (in Wh/kg) are plotted versus specific power density (in W/kg). In Figure 3.1, one can see the trade-off between energy density and power density. From fuel cells to supercapacitors by way of Li-ion batteries, energy density is decreasing in aid of power density.

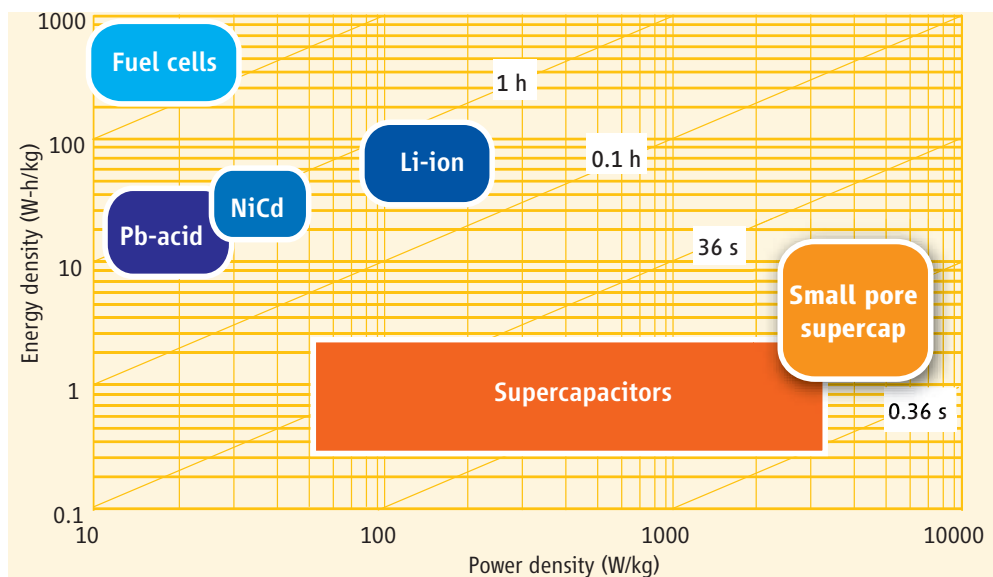


Figure 3.1: Ragone plot showing specific energy versus specific power for various energy-storing devices [14]

In order to answer the previous requirements, common energy storage types are analyzed and the most suited type for this work is detailed.

3.1 Primary batteries

Primary batteries are non-rechargeable, they thus have only one life cycle. However, they can sometimes still have their place in IoT applications when the power consumption and the sensor lifetime are particularly reduced. Primary batteries are mainly based on three technologies.

Zn-MnO₂ batteries

Zn-MnO₂ batteries are composed of a combination of metallic zinc (oxidation) and a manganese dioxide electrode (reduction). They exist under the form of zinc-carbon cells and alkaline batteries and differ according to the electrolyte inside.

The voltage window is between 0.9 V and 1.5 V. The energy density of a typical AA (approximately 8 cm³) zinc-carbon cell is 100 mWh/cm³, whereas a commercial alkaline cell reaches at present up to 400 mWh/cm³ [15].

These batteries are very well known and low cost, but present a high self-discharge rate.

Lithium primary batteries

Lithium primary batteries have an anode made of metallic lithium and a cathode made of several materials such as MnO₂ or FeS₂.

Batteries integrating MnO₂ commonly deliver a total cell voltage of around 3 V. These batteries work with the oxidation of lithium and reduction of manganese, with a typical energy density of 650 mWh/cm³.

The second type of lithium battery is based on FeS₂. It has a practical voltage of 1.5 V and is therefore compatible with alkaline and zinc-carbon cells. It has an energy density of approximately 550 mWh/cm³.

Overall, it is able to deliver high currents and has a quite flat voltage profile upon discharging. Moreover, it performs well at low temperatures and has a significantly lighter weight than alkaline cells.

Zn-air batteries

Zn-air batteries are a class of batteries that employ metallic zinc particles as its anode and an aqueous liquid electrolyte. With a voltage of 1.4 V, this battery is commercially available as button cells with an energy density of around 1500 mWh/cm³.

Other disadvantages of this type of battery are that the catalyst that is required for the reduction of oxygen usually consists of expensive noble metals and that the battery is unable to deliver high peak currents. This type of battery is therefore commonly used in applications where only low currents are required from a battery with a small volume [15].

3.2 Secondary batteries

Secondary batteries are rechargeable, they thus have a certain number of life cycles (usually more than 500). Only battery types that are suitable for the IoT domain are presented in this thesis.

Batteries with liquid or polymer gel electrolytes

Nickel metal hydride batteries

Nickel metal hydride batteries (NiMH) combine nickel at the positive electrode and hydrogen (metal hydride) at the negative electrode. During discharge, a proton, obtained from the electrolyte, occurs in reduction of nickel oxyhydroxide. The loss of protons in the electrolyte produces hydroxide anions which will recombine with a proton from the metal hydride.

The cells typically work at around 1.2 V, allowing interchangeability with alkaline batteries. However, they have a higher self-discharge rate and a narrow temperature window (0 to 45 °C). The energy density is around 250 and 380 mWh/cm³.

Li-ion batteries

Lithium-ion batteries are composed of lithium metal oxide at the positive electrode (LiCoO_2) and a material storing lithium in a neutral form such as graphite at the negative electrode. The charge process is based on the motion of lithium ions from the metal oxide to the electrolyte, where they are stored in graphite.

Compared to NiMH batteries, they have higher energy density (between 300 and 500 mWh/cm³), lower self-discharge rate and larger temperature window (-20 to 60 °C). They are however easily damaged in case of overdischarging or overcharging, thus requiring a special protective electric circuit for the power management.

Overall, liquid electrolytes (both NiMH and Li-ion) have high volatility and have been the source of explosions in lithium batteries. Research thus has been done on the design of solid electrolytes.

Solid-state batteries

Solid-state batteries use solid electrodes and a solid electrolyte, such as ceramics (e.g. oxides, sulfides, phosphates) or a solid polymer. They are potentially safer than batteries with liquid electrolytes, with higher energy density, but at a much higher cost. However, these efforts have faced a number of issues.

One of the biggest problems is that when the battery is charged up, atoms accumulate inside the lithium metal, causing it to expand. These repeated changes in the metal's dimensions make it difficult for the solids to maintain constant contact, and tend to cause the solid electrolyte to fracture or detach.

Another problem is that none of the proposed solid electrolytes are truly chemically stable while in contact with the highly reactive lithium metal, and they tend to degrade over time.

3.3 Supercapacitors

Supercapacitors are high-capacity capacitors storing energy in an electric field, rather than in a chemical reaction, like batteries. This allows high power density for short-term energy storage¹, almost instant recharging and very long lifetimes. Made of porous carbon (electrodes) and liquid salts (electrolyte) [16], they are not composed of harmful² chemicals or toxic metals. Since the supercapacitor is non-chemical, the voltage is free to rise until the dielectric fails (often in the form of a short circuit). It is thus needed to avoid going higher than the specified voltage, which is characterized by a lower voltage limit than for batteries.

Due to their behavior in between electrolytic capacitors and batteries, they are particularly well suited for IoT applications. Indeed, they typically store 10 to 100 times more energy per unit volume or mass than electrolytic capacitors. They can also accept and deliver charge much faster than batteries, and tolerate many more charge and discharge cycles than rechargeable batteries. Nevertheless, care needs to be paid to their significant leakage current which is proportional to the capacitance of the supercapacitor.

Instead of using a conventional solid dielectric, supercapacitors use electrostatic double-layer capacitance and electrochemical pseudocapacitance [17].

Electrostatic double-layer capacitors

Electrostatic double-layer capacitors (EDLCs) are the most common type of supercapacitors. They use carbon electrodes or derivatives with much higher electrostatic double-layer capacitance than electrochemical pseudocapacitance, achieving separation of charge in a Helmholtz double layer at the interface between the surface of a conductive electrode and an electrolyte.

Electrochemical pseudocapacitors

Electrochemical pseudocapacitors use metal oxide or conducting polymer electrodes with a high amount of electrochemical pseudocapacitance additional to the double-layer capacitance. They store charge chemically through redox reactions where one species transfers electrons to another, similar to a battery. While pseudocapacitors store more energy, their widespread use has been hampered by their narrow electrochemical voltage window, which is the voltage range where the electrode materials are stable.

Additionally, there exist hybrid capacitors, such as the lithium-ion capacitors, using electrodes with different characteristics: one exhibiting mostly electrostatic capacitance and the other mostly electrochemical capacitance.

3.4 New developments

Promising new methods are also developed in research laboratories, some of them are detailed hereafter.

¹They can provide very high currents during a short time.

²Failing in a nice way, they will never overrun or start a fire.

3D electrodes for electrochemical energy storage

Superior energy or power density for batteries is typically achieved only in ultra-thin electrodes with low mass loadings. To realize the full potential of these electrode materials, new electrode architectures allow more efficient charge transport beyond the limits of traditional electrodes. Working on the design and synthesis of 3D electrodes is promising to address charge transport limitations in thick electrodes. Such 3D porous architectures could enable composite electrodes with an unprecedented combination of energy and power densities [18].

In addition to the recent development of Li-ion batteries with flexible, bendable, or foldable characteristics, some research has been focused on batteries with advanced features of stretchability in which the systems are able to accommodate large mechanical strain and still maintain their functions. Such sponge-inspired electrodes for stretchable Li-ion batteries show no specific capacity reduction when bent, unlike the cells using conventional electrodes [19].

Lithium metal anode

Recent research has been achieved on lithium metal anodes that could improve the longevity and energy density of future batteries [20].

Most attempts to overcome the problems of solid-state batteries have focused on designing solid electrolyte materials that are absolutely stable against lithium metal, which turns out to be difficult. Instead, some researchers adopted an unusual design that utilizes two additional classes of solids, “mixed ionic-electronic conductors” (MIEC) and “electron and Li-ion insulators” (ELI), which are absolutely chemically stable in contact with lithium metal.

They developed a three-dimensional nanoarchitecture in the form of a honeycomb-like array of hexagonal MIEC tubes, partially infused with the solid lithium metal to form one electrode of the battery, but with extra space left inside each tube. When the lithium expands in the charging process, it flows into the empty space in the interior of the tubes, moving like a liquid even though it retains its solid crystalline structure. This flow, entirely confined inside the honeycomb structure, relieves the pressure from the expansion caused by charging, but without changing the outer dimensions of the electrode or the boundary between the electrode and electrolyte. The other material, the ELI, serves as a crucial mechanical binder between the MIEC walls and the solid electrolyte layer.

3.5 Shape

In addition to the electrical and thermal characteristics, the form of the storage element is particularly important for IoT devices where the full sensor size is often limited. The main trade-off thus appears between the charge capacity and the size of the energy storage element.

The main shapes of micro-batteries are button cells, pouch cells and thin film batteries.

3.6 Comparison

Table 3.1 presents the main figures of merit for the previously described types of energy storage.

	Capacitors			Batteries		
	Ceramic	Electrolytic	Supercap EDLC	Non-rechargeable Alkaline	NiMH	Rechargeable Lithium ion
Power density [W/g]		> 100	2 – 10		2.5 – 10	1 – 3
Energy density [mWh/g]	0.1 [21]	0.01 – 0.3	5		60 – 120	120 – 240
Self-discharge rate [per month]	100%	100 h	50%	< 0.3%	0.08 – 2.9%	5%
Leakage current	1 – 100 nA/pF		2 – 5 fA/pF [22] [23]			5 µA [21]
Service life [years]	25 [21]	15	10 – 15	5 – 10		5 – 10
Life cycles	unlimited [21]	unlimited	1 000 000	1	180 – 2000	500
Degradation	negligible		-80% in 10 years			-50% in 500 cycles
Charge time			1 – 10 s			10 – 60 min
Cell voltage [V]		4 – 630	2.3 – 2.75	1.5	1.2	3.6
Charge T° [°C]		-40 – 70	-40 – 65			0 – 45
Discharge T° [°C]		-40 – 70	-40 – 65			-20 – 60
Discharge efficiency		99%	95%		66% – 92%	90%
Toxicity			low			middle

Table 3.1: Comparison of various types of energy storage

In this table, the life cycle is the number of complete charge/discharge cycles that the battery is able to support before its capacity falls under 80% of its original capacity. Although the deployment of such sensors would imply the fabrication of several thousands of energy storage elements, the impact of the toxicity is small for such projects lasting more than 20 years without replacement. The degradation corresponds to the decrease of its maximum energy storage throughout its life.

Another factor of merit is the overall efficiency, which is computed as

$$\eta = \frac{E_O}{E_I}$$

where E_O is the energy delivered during the whole life of the energy storage element, and E_I is the total energy fed to the storage element, composed of both the fabrication energy and the recharge energy. It is difficult to compute this efficiency due to the lack of information about the fabrication energy (typically not given by manufacturers). However, Li-ion batteries (50.17 kWh/kg for electric vehicles [24]) generally require more manufacturing energy than supercapacitors.

Criticality

To assess the criticality of energy storage elements, one needs to consider the environmental and societal impacts combined with their scarcity. The scarcity of an element is assessed by the variation of its availability on Earth between the past decades and nowadays (not to be confused with rare-earth elements which are not critical). They include components overused for electronic devices such as copper, gold, silver, lithium and cobalt.

For Lithium-ion and NiMH batteries, the following compounds are used:

- Positive electrode: metal oxide compounds such as lithium extracted from brine or rock, nickel, cobalt, hydrogen-absorbing alloy (nickel alloys with many metals: V, Ti, Zr, Ni, Cr, Co, Al and Fe)
- Negative electrode: graphite (carbon-based)

- Electrolyte

One can thus see that many critical and polluting compounds appear in the positive electrode.

For EDLCs, the following compounds are used:

- Electrodes: porous carbon (activated carbon, carbon nanotubes and carbon aerogels) built from graphite [25]
- Electrolyte: liquid salts (water with ions)
- Polymeric membrane forming a microporous layer as separator

Supercapacitors are thus mainly built from carbon, one of the most abundant elements on Earth. They are far less toxic and resource-intensive than metal-based batteries.

3.7 Selection

Building upon these results, a supercapacitor is chosen because of its high lifetime, low toxicity, low criticality and reasonable energy density. As detailed in the Ragone plot (Figure 3.1), this energy storage element can deliver high currents but stores less energy per volume. Its substantial leakage current is also needed to be further taken care of. The sizing of this supercapacitor will be achieved in Chapter 7.3 once the whole power consumption is fully determined.

Chapter 4

Power management

The purpose of power management is to harvest energy from solar cells, store it in a supercapacitor, and deliver it to the circuit through a stable voltage supply. In this section, the best supply voltage is determined and the power management unit is explained.

4.1 Operating voltage design

First, the supply voltage is used to power the sensing subsystem and the MCU/transceiver chip. For practical and energy efficiency reasons, the same supply voltage is selected for the whole system.

Since the microcontroller uses a low-dropout (LDO) regulator to regulate its internal voltage, the current consumption is independent from the supply voltage. In order to minimize the power consumption, one thus needs to use the lowest supply voltage. However, using a low supply voltage decreases the AFE amplification gain and therefore the precision (i.e. the signal-to-noise ratio) on the microphone signal that will be read at the input of the MCU. Indeed, while the noise at the sensing output is roughly independent from the amplification gain of the sensing subsystem (see the proof in Section 5.2), the signal power is reduced with the gain. Hence, this trade-off leads to the selection of a 2.5 V supply voltage which lies in the 2.2 V – 3.6 V range of the CMWX1ZZABZ chip.

4.2 Power management unit

A power management unit (PMU) is an integrated energy management circuit that extracts DC power from solar cells to simultaneously store energy in a rechargeable element and supply the system with independent regulated voltages. An AEM10941 chip from e-peas is selected because of its ultra-low power consumption and the close relations between the university and the company (see Figure 4.1).

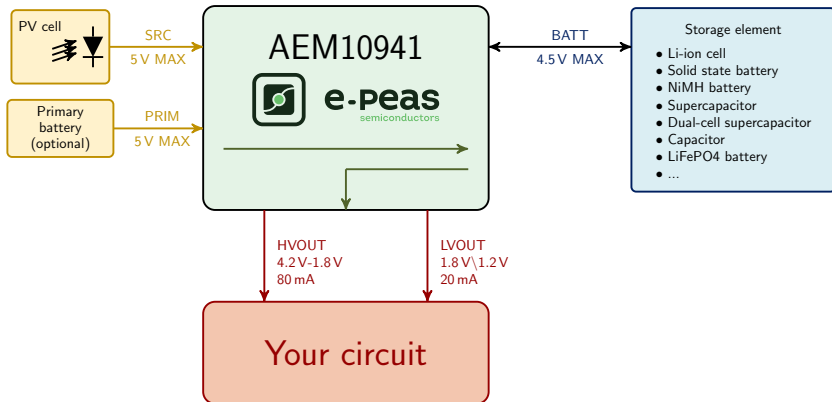


Figure 4.1: AEM10941 simplified schematic view [26]

Its characteristics are given in Table 4.1, by only considering the high voltage regulator. The very low quiescent current is nearly independent from the supercapacitor voltage.

Max input current	110 mA
Max input voltage	5 V
Output voltage	1.8 V – 4.1 V
Max output current	80 mA
Max supercap charge	4.5 V
Min dropout supercap – output voltage	0.3 V
Quiescent current	0.6 μ A

Table 4.1: Characteristics of the AEM10941 PMU

Storage element and LDO configuration

Configuration pins determine various operating modes by setting predefined conditions for the energy storage element (overcharge or overdischarge voltages) and by selecting the voltage of the high-voltage supply and the low-voltage supply. The low-voltage supply is not used and the high-voltage supply is set to 2.5 V. These characteristics correspond to a preset state in the chip, which helps reduce internal losses by not using additional resistors to select a custom configuration. The three configuration pins CFG[2], CFG[1] and CFG[0] are thus set to 0, 1 and 1, corresponding to the charge of a dual-cell supercapacitor charged in the range 2.8 V – 4.5 V in order to power the low-voltage and high-voltage supplies at 1.8 V and 2.5 V, respectively.

Additionally, three status pins allow monitoring the PMU, whose one informs about supercapacitor overdischarge. For a first prototype, connecting this pin to a LED can be useful to deduce the supercapacitor state, but it is not used in the final model to further reduce power consumption (which is non-negligible for typical LEDs, around 1 mA).

Maximum power point tracking

The efficiency of power transfer from the solar cell depends on both the amount of sunlight arriving on the solar cells and the electrical characteristics of the load. As the amount of sunlight varies, the load characteristic that produces the highest power transfer efficiency changes, so that the efficiency of the system is optimized when the load characteristic changes to keep the power transfer at highest efficiency. Maximum power point tracking (MPPT) is thus used by the PMU by means of a boost converter regulating its input voltage so that the electrical current that enters the boost converter yields the best power transfer from the harvester under any ambient conditions (see Section 7.2 for more details about the intrinsic principle of solar cells).

This PMU uses the open-circuit voltage algorithm, the simplest MPPT control method. It consists to set the voltage at a constant ratio of the open-circuit voltage V_{OC} . By temporarily disconnecting the source from the PMU, the MPPT module maintains knowledge of V_{OC} . It then sets the MPPT voltage at V_{MPPT} depending on V_{OC} and the ratio (70%, 75%, 85% or 90%) selected in hardware via two headers connected to the configuration pins. A typical MPPT ratio leading to the maximum power is 76% [27], but it will be refined experimentally in the validation section. Still, the main disadvantage of this method is that there is momentary power loss due to the disconnection of the load from the solar cells for the sampling of its open-circuit voltage.

Boost conversion efficiency

The energy converted from the solar cells to the supercapacitor (called boost voltage) is not fully converted due to the internal boost converter efficiency. As depicted in Figure 4.2 for a typical harvested current of 10 mA, the efficiency is maximum when the input voltage V_{SRC} is 0.4 V below the output voltage V_{BOOST} (see Table 4.2).

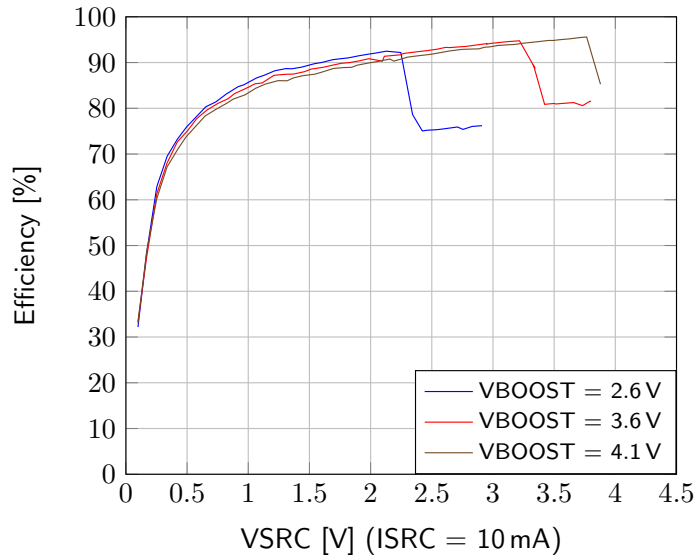


Figure 4.2: Boost conversion efficiency (solar cells – supercap) of the AEM10941

V_{SRC}	V_{BOOST}	Efficiency
2.2 V	2.6 V	92%
3.2 V	3.6 V	95%
3.7 V	4.1 V	96%

Table 4.2: Values of maximum efficiency for the src – boost conversion with a 10 mA input current

Since the source voltage impacts both the boost conversion efficiency and the harvested power (see previous paragraph), the optimal source voltage needs to be determined. Based on Figure 4.2, the efficiency significantly falls when the source voltage exceeds its optimal voltage. The source voltage thus needs to stay below $V_{BOOST} - 0.4$ V at all times, corresponding to 2.4 V for this work (supply voltage of 2.5 V implying a supercap voltage of at least 2.8 V). In this case, it is thus expected to reach a boost efficiency of 92% whatever the supercap voltage. Finally, the maximum source voltage set to 2.4 V might be slightly relaxed if the IV curve of the solar cells provide a significant power increase at a higher source voltage (see Section 7.2).

High-voltage LDO regulation

As shown in Figure 4.3, the PMU supply voltage depends on the load current drawn by the sensing and MCU/RF subsystems. It decreases from 2.5 V without load to 2.43 V at the maximum load (that is, 80 mA). Although this voltage variation might impinge upon the signal reading at the ADC input of the microcontroller, no voltage regulation needs to be taken into account inside the MCU code. Indeed, both the signal voltage $V_{in,ADC}$ from the microphone and the ADC supply voltage V_{DD} vary likewise, this leads to the same digitized number $\lfloor V_{in,ADC}/V_{DD} \rfloor$.

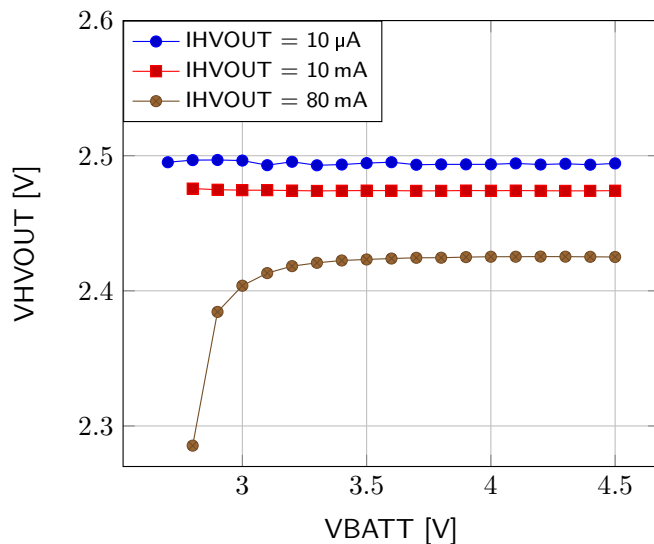


Figure 4.3: High-voltage LDO regulation at 2.5 V in function of the load current

Finally, the LDO efficiency can be simply calculated as $V_{\text{out}}/V_{\text{in}}$ (same input – output current) if the quiescent current ($0.6 \mu\text{A}$) can be neglected with regards to the output current. The hyperbolic curve in Figure 4.4 confirms the $1/V_{\text{in}}$ dependence of the efficiency on V_{in} . It is thus advised to work at the lowest supercap voltage (i.e. 2.8 V) by selecting a supercapacitor with a similar operation voltage range.

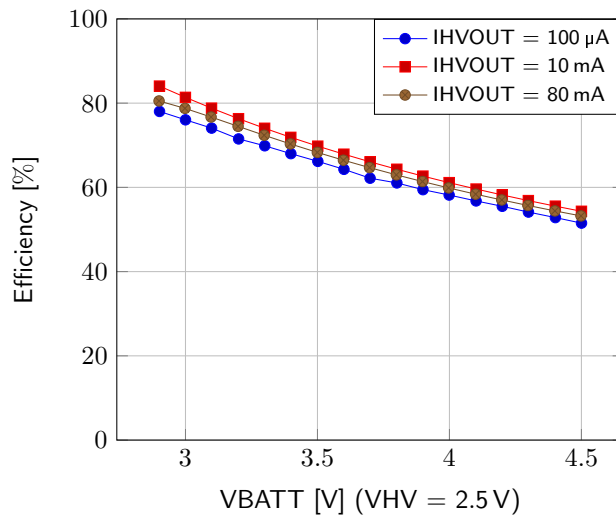


Figure 4.4: High-voltage LDO efficiency at 2.5 V in function of the load current

Chapter 5

Sensing subsystem

Sound waves are generated by the variation of a physical characteristic, the pressure. This deviation propagates via vibrations in the environment in such a way that sound can be measured by a microphone from a distance of the source.

Sound waves are often described in terms of sinusoidal plane waves (see Figure 5.1). Hence, they have a direction of propagation, a speed v , a frequency f and an amplitude A .

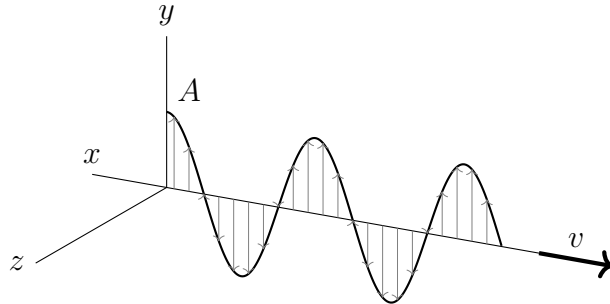


Figure 5.1: General sound wave description

The amplitude of sound pressure corresponds to the loudness of a sound and is typically expressed as the root mean square (RMS) amplitude, called sound pressure level (SPL). Let the RMS sound pressure be $p = A/\sqrt{2}$ for sine waves, the SPL amplitude is given by

$$L_p = 20 \log_{10} \left(\frac{p}{p_0} \right) \simeq 20 \log_{10}(p) + 94 \quad [\text{dB}_{\text{SPL}}]$$

where $p_0 = 20 \mu\text{Pa}$ is the reference RMS pressure (hearing threshold of humans at 1 kHz).

Additionally, the sound SPL amplitude changes over the distance (from r_1 to r_2) according to the propagation law of spherical waves:

$$L_{p2} = L_{p1} + 20 \log_{10} \left(\frac{r_2}{r_1} \right) \quad [\text{dB}_{\text{SPL}}].$$

Table 5.1 gives typical sound pressure levels.

Source of sound	Distance	Sound pressure [dB]
Jet engine	1 m	150
Trumpet	0.5 m	120
Traffic on busy road	10 m	90
Passenger car	10 m	70
Quiet room	ambient	25

Table 5.1: Typical sound pressure levels

In this work, the sensor is required to detect the song of a bird (around 50 dB_{SPL} at 1 m of the source) located 50 m away. The minimum detected sound pressure is thus

$$L_{p_{\min}} = 50 - 20 \log_{10}(50) = 16 \text{ dB}_{\text{SPL}}.$$

Sound production from several bird species have been measured up to 95 dB_{SPL} and are generally greater for larger birds [28]. The sensor thus needs to detect sounds of at least

$$L_{p_{\max}} = 95 - 20 \log_{10}(50) = 61 \text{ dB}_{\text{SPL}}.$$

The frequency range of human hearing is often reported to be between 20 and 20 000 Hz, but the ability to hear higher frequencies decreases with age. For this reason, a correction, called A-weighting, is applied to instrument-measured sound levels to account for the relative loudness perceived by the human ear as a function of the frequency (see Figure 5.2).

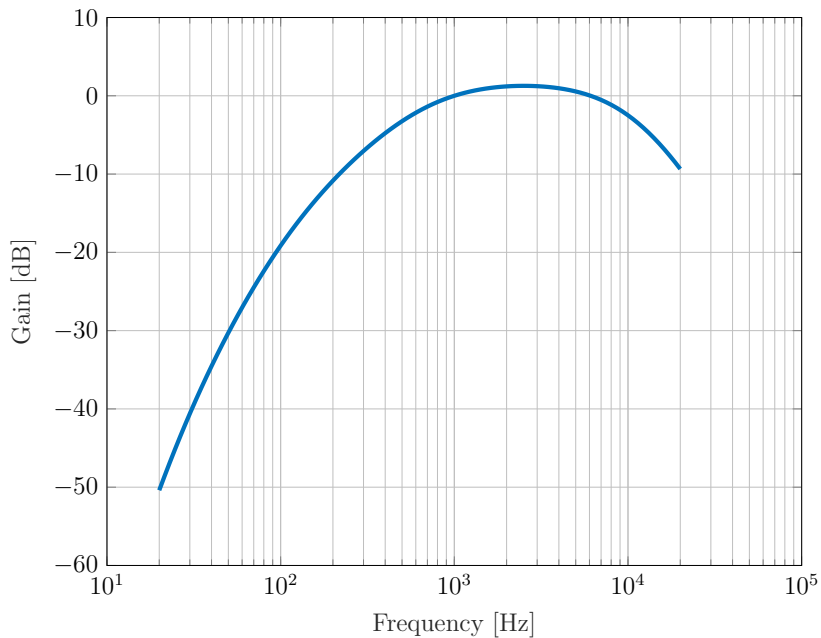


Figure 5.2: A-weighting curve

Many bird songs have frequency ranges between 1 kHz and 8 kHz, which places them in the spot

of human hearing. However, some birds can produce sounds at frequencies¹ as low as 23 Hz [29] or as high as 15 kHz [30]. Since the presented sensor aims to mainly analyze bird sounds, it has to match the frequency specifications ranging between 20 Hz and 20 kHz.

In the end, the characteristics of the sound wave at the sensor are summed up in Table 5.2.

Pressure range	16 – 61	dB _{SPL}
Frequency range	20 – 20000	Hz

Table 5.2: Sound wave characteristics at the sensor

As depicted in Figure 5.3, the sensing subsystem is composed of a microphone and a signal conditioning circuit called analog front-end. This block handles the signal transmission from the input sound pressure detected by the microphone to an analog voltage $V_{\text{mic,ADC}}$ further processed by a microcontroller.

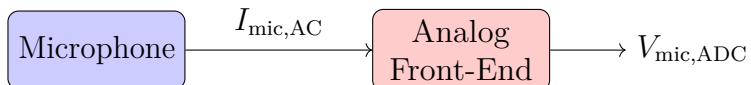


Figure 5.3: Block diagram of the sensing subsystem

5.1 Microphone

A microphone is a device that converts sound into an electrical signal (also called transducer). Generally, they mimic the inner workings of human ear by using a diaphragm which vibrates with the sound pressure. There exist several types of microphones for which the most important characteristics, called figures of merit, need to be compared.

Main types of microphone

Microphones are categorized by their transducer principle, corresponding to the way they detect the variation of input sound pressure.

Carbon microphones

Carbon microphones were the first created type of electrical microphone. They are based on the variation of electrical resistance between two plates due to the motion of a diaphragm on one of these plates. This type of microphone is less used because of its limited frequency response and high noise level (background and crackling noise [31]).

¹One might also want to assess the impact of moving birds on the frequency. For this purpose, the Doppler effect characterizes the frequency f perceived at the sensor node compared to the emitted frequency f_s of the bird when it moves at speed v_s . The relative variation of frequency is given by $f/f_0 = \frac{v}{v \pm v_s}$ where v is the sound velocity (343 m/s in ambient conditions). For a typical bird velocity (12 m/s), the equation provides a relative variation of $\pm 4\%$, which corresponds to a small (but non-negligible) impact on the perceived frequency.

Optical microphones

Optical microphones use the moving diaphragm as a reflection plate for the light of a laser. The intensity of the light, depending on the deformation of the diaphragm, is converted to an electrical signal through a photodiode. Their high power consumption (more than 5 mW, 5.4 mW in [32]) prevents them from being used in IoT applications.

Condenser microphones

Condenser microphones are based on a parallel-plate capacitor for which one of the plates is the diagram. For a fixed charge Q on the capacitor, the voltage across the capacitor varies with the capacitance according to

$$V = \frac{Qd}{\varepsilon A}$$

where s is the distance between the plates, A is the area of the plate, and ε is the electric permittivity of the medium inside the plates.

This type can be further divided in active and passive condenser microphones.

Active condenser microphones require biasing circuitry to charge the capacitor and perform first stage amplification. In this group belong microelectromechanical systems (MEMS) microphones which are small package condenser microphones made using semiconductor production techniques. Typically, they already integrate an ADC inside. The small size and the rather low power consumption (10 μ W to 1 mW [33], [34]) of MEMS microphones are ideal for IoT applications.

Passive condenser microphones do not require biasing of the capacitor. For instance, condenser electret microphones have an electret material as diaphragm, a material that has a permanent electrical charge on it. Passive microphones are also appealing for their low power consumption and reduced complexity.

Piezoelectric microphones

Piezoelectric microphones directly translate the sound pressure into a voltage by means of a piezoelectric crystal, which redistributes the charges in the crystal under a deformation. They can be packaged in MEMS microphones and have a low power consumption (about 300 μ W [35]). However, their high impedance makes them sensitive to electrostatic pick-up of hum², which decreases its performance in the presence of mains-powered audio equipment or AC electromagnetic fields from nearby appliances.

Inductive microphones

Inductive microphones are passive microphones working via electromagnetic induction. The vibrations of the diaphragm move a permanent magnet through a coil, inducing an electrical current. They are generally less sensitive, especially at picking up high frequencies and short, detailed sounds. They are also unable to pick up distant sounds laterally and from the back of the microphone, which may lead to flatter audio (unidirectionality). They are thus not suited for this application.

²Mains hum is a sound associated with alternating current at the frequency of the mains electricity (50 Hz).

Figures of merit

In order to select the most suited type of microphone for this application, one has to characterize the main figures of merit related to a microphone.

Power consumption

For both active and passive microphones, the operation current and voltage are of essential importance in IoT applications. The standard operation voltage V_{mic} (also called bias voltage) is the voltage needed by the microphone to operate with full functionality, so that the microphone can amplify and record signals fully. The maximum current consumption is often specified to provide a rough upper limit. However, one is more interested in the measurement of the microphone IV curve which allows deducing the operation current I_{mic} at the operation voltage.

Sensitivity

Sensitivity is the electrical response at the microphone output to a given standard acoustic input. The standard reference input signal for microphone sensitivity measurements is a 1 kHz sine wave at 94 dB_{SPL}, or 1 Pa. It is expressed in V/Pa or in dB.

Signal-to-noise ratio

In the microphone's framework, the signal-to-noise ratio (SNR) specifies the ratio of a reference signal to the noise level of the microphone output. Brought back to the input, the SNR is the difference in decibels between a standard 1 kHz, 94 dB_{SPL} reference signal and the microphone pressure noise³. It is an image of the noise generated inside the microphone, called self-noise. Expressed in dB_{SPL}, the self-noise acts like a theoretical external noise source placed at the input of an ideal microphone. The relation between the self-noise and the SNR is thus given by

$$\text{SNR} = 94 - \text{self-noise} \quad [\text{dB}].$$

The SNR is calculated by measuring the noise output of the microphone in a quiet, anechoic environment. This specification is typically presented over a 20 kHz bandwidth as an A-weighted value.

Frequency response

The frequency response describes the output level across the frequency spectrum. The high and low frequency limits are described as the points at which the microphone response is 3 dB below the reference output level at 1 kHz, which is customarily normalized to 0 dB. As for the SNR, the frequency response characterization requires precise measurements in anechoic chamber. Typical microphone frequencies lie in the human hearing range.

³The microphone SNR is independent from the input sound pressure. It should not be confused with the typical definition of the SNR, which provides the power ratio between the input signal and the noise at a specific stage of a conditioning chain.

Directionality

Directionality describes the pattern in which the microphone sensitivity changes when the sound source changes position in space. Most of the analyzed microphones are omnidirectional.

Finally, the main figures of merit associated with a microphone are summarized below:

- I_{mic} : rated current (in A),
- V_{mic} : rated voltage (in V),
- S : sensitivity from the input sound pressure to the output voltage (in dB),
- SNR_{mic} : signal-to-noise ratio (in dB),
- the frequency range (in Hz),
- the directionality,
- and the operating temperature (in °C).

Microphone type selection

IoT devices are limited by their size, cost and energy requirements. Table 5.3 quantitatively summarizes the two main characteristics for each type of microphone.

Type	Reference	Noise [dB _{SPL}]	Power cons. [μW]
Condenser (MEMS)	ICS-40720	24	570
Condenser (Electret)	AOM-5024L-HD-R	14	420
Piezoelectric	PMM-3738-WP-R	33	300

Table 5.3: Comparison of several types of microphone

A piezoelectric microphone is not considered due to its sensitivity to electrostatic pick-up of hum. MEMS and electret condenser microphones are very similar and well suited for this application, but MEMS microphones already have the amplification circuit inside. Finally, an electret condenser microphone is selected for this work since it allows a precise design of the amplification circuit, optimizing the whole noise and power consumption.

Electret condenser microphone selection

Considering the main figures of merit stated above, Table 5.4 compares several state-of-the-art electret condenser microphones.

The AOM-5024L-HD-R microphone has been selected since it surpasses the others in terms of the most important parameters, the self-noise (related to the SNR) and the sensitivity, while roughly keeping the same power consumption. With its self-noise of 14 dB_{SPL}, it is in fact the only microphone that allows staying below the 16 dB_{SPL} limit for the minimum detectable sound wave.

	ABM-707-RC	CMC-6027-24L100	AOM-5024L-HD-R
Current [μA]	500	500	500
Voltage [V]	1.5	2	2
Sensitivity [dB]	-41	-24	-24
SNR [dB]	60	70	80
Output impedance [Ω]	2.2	2.2	2.2
Frequency range [Hz]	50 – 16000	100 – 20000	20 – 20000
Temperature [°C]	-20 – 60	-20 – 70	-30 – 70

Table 5.4: Comparison of several electret condenser microphones

However, one has to characterize more precisely the current and voltage characteristics because the values given in the datasheets are very general (current of $500 \mu\text{A}$ and voltage of 2 V). The IV curve of the AOM-5024L-HD-R and the ABM-707-RC⁴ is given in Figure 5.4.

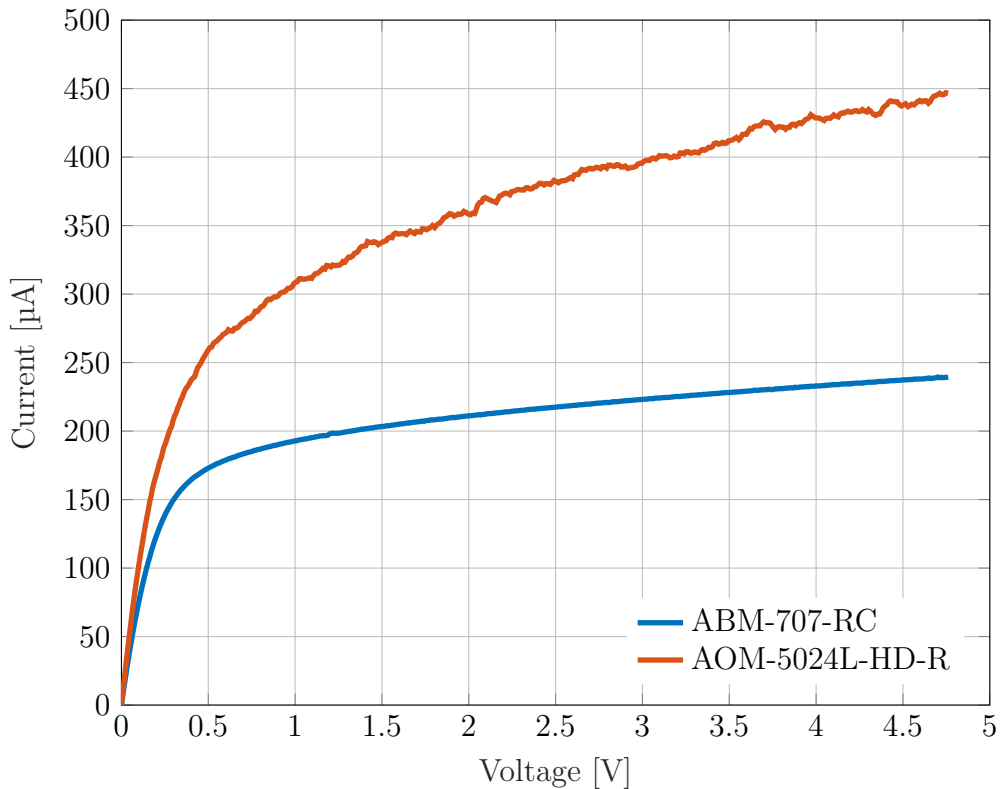


Figure 5.4: IV curve of several microphones

In order to select the best operating voltage, one has to find a trade-off between keeping a low voltage (and thus a low power consumption) and having a sufficient sensitivity by retaining the microphone transistor in saturation. Finally, the operating point given in Table 5.5 for the AOM-5024L-HD-R will be considered in the following. One can sadly notice a power

⁴The ABM-707-RC, which was initially available in the laboratory, served as a first measurement to characterize the microphone and the analog front-end.

consumption slightly higher than the reference microphone, this model remains the best suited because of his high precision (the self-noise of the reference microphone is too high to be considered in this work).

Current	I_{mic}	358 μA
Voltage	V_{mic}	2 V

Table 5.5: Operating point of the AOM-5024L-HD-R microphone

5.2 Analog front-end

Once the microphone type is selected, one can analyze in more detail the working principle of electret microphones. The voltage variation across the electret capacitor varies with the capacitance, acting as an AC-coupled voltage source. Because the charge on the microphone capacitor must be fixed, the amplifier circuitry directly in contact with it must have extremely high input impedance, such that no charge can flow through the amplifier circuit.

For this reason, most electret microphones have an internal junction field-effect transistor (JFET) which buffers the microphone capacitor. The voltage signal produced by sound modulates the gate voltage of the JFET (V_G), causing a change in the current flowing between the drain and source of the JFET (I_{mic}). An extremely high resistance may be included to bias the gate of the JFET, but parasitic resistance in the microphone PCB will be sufficient in this work.

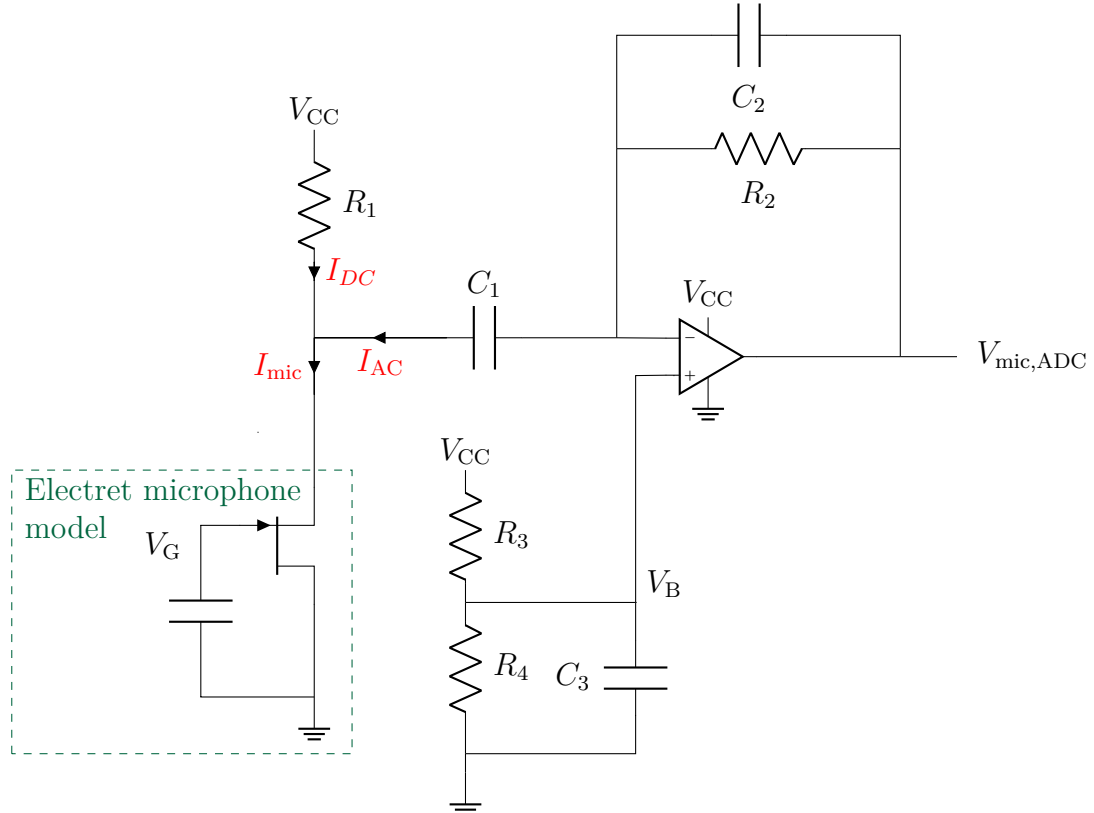


Figure 5.5: Microphone and analog front-end circuit

The amplification circuit presented in Figure 5.5 is typical for condenser electret microphones [36]. It allows converting the microphone current I_{AC} into an output voltage $V_{\text{mic,ADC}}$ which sweeps the input of a further ADC.

The current in the microphone I_{mic} has a DC component (I_{DC} , characterized in the previous section) necessary to put the internal JFET in the saturation region, and an AC component (I_{AC}) caused by sound waves. If the impedance of capacitor C_1 is much less than R_1 at audio frequencies, then I_{AC} will flow through C_1 and not R_1 . The op-amp acts as a transimpedance amplifier, and attempts to hold its inverting input at a constant voltage V_B by varying its output. The resistors and capacitors of the circuit will be further designed such that, in the audio sound frequency band, C_2 and C_3 are open-circuited, and C_1 is short-circuited. In this case, the output voltage of the op-amp is simply given by

$$V_{\text{mic,ADC}} = R_2 I_{\text{AC}} + V_B \quad [\text{V}]$$

in this frequency band (see Appendix A for details).

Because capacitor C_1 is chosen to have a very low impedance at audio frequencies, the voltage at the drain of the microphone JFET (V_{DS}) varies very little, potentially reducing distortion caused by channel length modulation in the JFET. This makes the circuit very convenient since the drain current I_{mic} only depends on the JFET gate voltage V_G , and not the constant voltage V_{DS} (due to the channel length modulation, also called Early effect).

Designing this amplification circuit requires more attention than for the microphone since it induces consequent noise which is mainly due to the operational amplifier. The next computations will introduce a trade-off between the noise reduction and the power consumption of common operational amplifiers.

Amplification circuit design

The parameters of the AOM-5024L-HD-R microphone selected for this design are summed up in Table 5.6 with the experimental current measurements.

Op. current	I_{mic}	358 μA
Op. voltage	V_{mic}	2 V
Sensitivity	$S_{\text{mic,dB}}$	-24 dB
SNR	SNR_{mic}	80 dB
Impedance	R_L	2.2 k Ω
Frequency range		20 Hz – 20 kHz
Temperature		-30 °C – 70 °C

Table 5.6: Characteristics of the selected microphone: AOM-5024L-HD-R

The microphone self-noise is given by $p_{\text{SN,dB}} = 14 \text{ dB}_{\text{SPL}}$ and $p_{\text{SN}} = 100 \mu\text{Pa}$. Since the microphone outputs a current (and not a voltage) depending on the input pressure, a load impedance R_L has been used to convert the current sensitivity towards the voltage sensitivity.

Gain calculation

First, the dB value of the sensitivity must be converted to a linear value, which is

$$S_{V,\text{mic}} = 10^{S_{\text{mic},\text{dB}}/20} = 63.1 \text{ mV/Pa}$$

expressed in volts per Pascal of air pressure.

Because the preamplifier is a transimpedance type, this must be converted to a value of current per Pascal of air pressure. It can be converted thanks to the microphone impedance, which was used to measure the microphone sensitivity. The output current per Pascal of air pressure is

$$S_{I,\text{mic}} = \frac{S_{V,\text{mic}}}{R_{L,\text{mic}}} = 28.7 \mu\text{A/Pa}.$$

Then, one has to map the minimum detected input sound pressure to the minimum detected output voltage of the amplifier.

The minimum input sound pressure, determined at the beginning of the chapter, is given by

$$L_{p,\text{min}} = 16 \text{ dB SPL} \Rightarrow p_{\text{min}} = p_0 10^{L_{p,\text{min}}/20} = 126 \mu\text{Pa},$$

which is expressed in RMS value. It corresponds to a minimum drain current in the microphone of

$$I_{\text{mic,min,RMS}} = S_{I,\text{mic}} p_{\text{min}} = 3.63 \text{ nA}.$$

The minimal output voltage depends on the ADC resolution of the microcontroller unit. The STM32L072 has a 12-bit resolution and the operating voltage V_{CC} is 2.5 V (see Section 4.1). The ADC voltage resolution is thus

$$V_{\text{ADC,res}} = \frac{V_{CC}}{2^{12}} = 610 \mu\text{V}.$$

In order for the input signal to be read with sufficient precision (6 bits) by the ADC, it has to vary higher than $2^6 V_{\text{ADC,res}}$. Based on Figure 5.6, one can deduce the minimum RMS voltage:

$$2^6 V_{\text{ADC,res}} = 2\sqrt{2} V_{\text{ADC,RMS}} \Rightarrow V_{\text{ADC,RMS}} = 2^4 \sqrt{2} V_{\text{ADC,res}} = 13.8 \text{ mV}$$

or $V_{\text{ADC,RMS}} = -37.2 \text{ dBV}$.

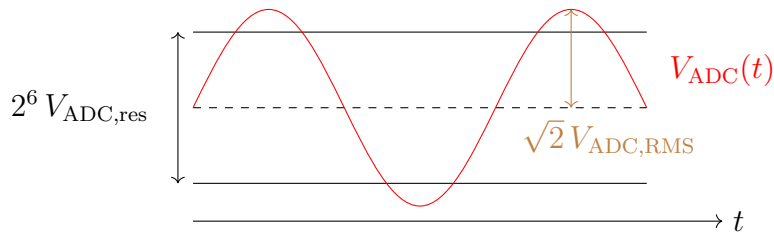


Figure 5.6: Resolution and RMS values of ADC voltage

Then, one can compute the transimpedance gain, which maps the RMS values of the input current to the output voltage:

$$R_2 = \frac{V_{\text{ADC,RMS}}}{I_{\text{mic,min,RMS}}} = 3.81 \text{ M}\Omega.$$

The maximum microphone RMS current appears when the ADC voltage is maximum:

$$I_{\text{mic,max,RMS}} = \frac{V_{\text{CC}}/(2\sqrt{2})}{R_2} = 232 \text{ nA},$$

corresponding to a maximal input sound pressure of

$$p_{\text{max}} = \frac{I_{\text{mic,max,RMS}}}{S_{I,\text{mic}}} = 8.1 \text{ mPa} \quad \Rightarrow \quad L_{p,\text{max}} = 20 \log_{10} \left(\frac{p_{\text{max}}}{p_0} \right) = 52.1 \text{ dB}_{\text{SPL}}.$$

The input spreads from 16 dB_{SPL} to 52.1 dB_{SPL}, giving a variation of 36.1 dB. It is worth noting that, when expressed in dB, the input variation is exactly equal to the 6-bit output variation⁵ since

$$20 \log_{10} (2^6) = 36.1 \text{ dB}.$$

Thereby, there is a trade-off between the number of bits dedicated to the minimum ADC signal (6 bits) and the input pressure range (6 bits) since they sum to the ADC resolution (12 bits). Still, the maximum input sound pressure of 52.1 dB_{SPL} suits quite well the requirements of this work, for which a louder sound is rarely produced by birds (about 60 dB_{SPL} at the source [37]).

Figure 5.7 depicts the three main variables of the sensing subsystem expressed in dB scale: the input sound pressure p , the microphone voltage V_{mic} and the output voltage V_{ADC} . The output ADC voltage has been fixed by the microcontroller specifications. The minimum input sound pressure, expressed both in dB and dB_{SPL}, has then been mapped to the minimum ADC voltage. In turn, it fixed the maximum input sound pressure since the input pressure range has the same length as the output voltage range previously set.

The only remaining degree of freedom for the microphone and amplification circuit lies in the relative position of the scale in between, characterizing the microphone voltage V_{mic} . This voltage is obtained from the input sound through the microphone sensitivity $S_{\text{mic,dB}}$, and is converted to the ADC voltage through the voltage gain of the amplification circuit:

$$G_{V,\text{dB}} = \frac{V_{\text{ADC,RMS}}}{V_{\text{mic,RMS}}} = \frac{R_2 I_{\text{mic,RMS}}}{V_{\text{mic,RMS}}} = \frac{R_2}{R_L} \quad [\text{dB}].$$

Since the input/output relation is given by

$$\begin{aligned} p_{\text{dB}} + S_{\text{mic,dB}} + G_{V,\text{dB}} &= V_{\text{ADC,RMS}} \quad [\text{dB}], \\ 16 \text{ dB} - 94 \text{ dB} + S_{\text{mic,dB}} + G_{V,\text{dB}} &= -37.2 \text{ dB}, \end{aligned}$$

the scale of the microphone voltage needs to be adapted according to

$$S_{\text{mic,dB}} + G_{V,\text{dB}} = 40.8 \text{ dB}.$$

This relation is useful for a parallel optimization of both the microphone and amplification circuit aiming at selecting the best noise/current consumption characteristic. However, the previous microphone selection has fixed the sensitivity at -24 dB and directly leads to a voltage gain of 64.8 dB.

⁵This is the difference between the bit resolution of the ADC (12) and the number of bits used for the minimum detectable signal (6).

Finally, the figure highlights that the self-noise for this microphone ($14 \text{ dB}_{\text{SPL}}$) is below the minimum input sound pressure. Brought back to the input pressure domain, the AFE noise will also be computed and added to this intrinsic microphone noise.

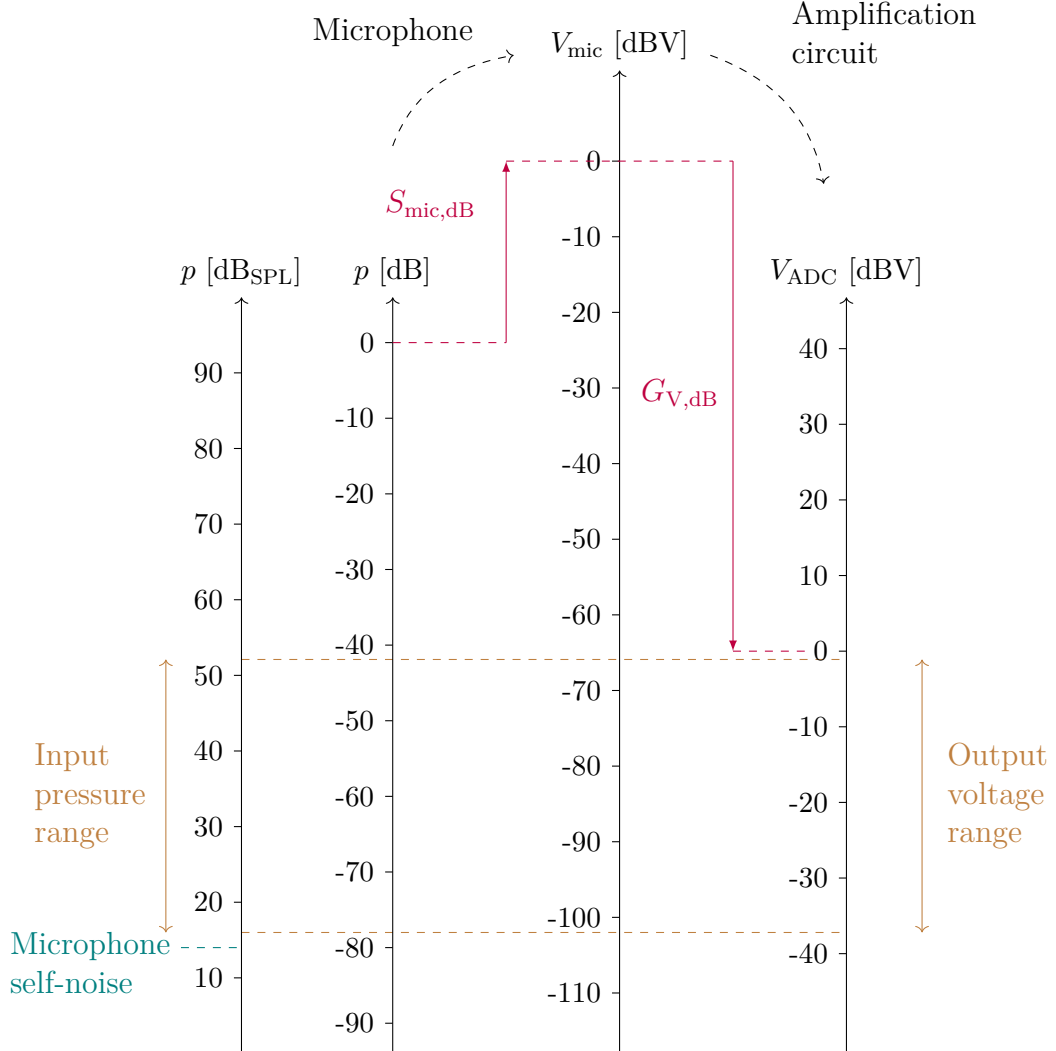


Figure 5.7: Range of p , V_{mic} and V_{ADC} along the dB scale

The feedback capacitor C_2 compensates for parasitic capacitance at the op-amp inverting input which can cause instability. It also forms a high frequency pole with resistor R_2 in the response of the amplifier. According to the frequency range specified for the input sound pressure, the frequency of this pole must be $f_H = 20 \text{ kHz}$. The feedback capacitor value can then be calculated as

$$C_2 = \frac{1}{2\pi f_H R_2} = 2.09 \text{ pF.}$$

Microphone bias resistor and coupling capacitor

The internal JFET of the electret microphone being biased by resistor R_1 , the value of this resistor can be calculated from the desired supply voltage (V_{CC}), the microphone operating

voltage (V_{mic}) and the current consumption (I_{mic}):

$$R_1 = \frac{V_{\text{CC}} - V_{\text{mic}}}{I_{\text{mic}}} = 2.38 \text{ k}\Omega.$$

Resistor R_1 and capacitor C_1 form a high-pass filter, the corner frequency of this filter must be low enough not to attenuate low-frequency sound waves. As specified in the input frequency range, a corner frequency of $f_L = 20 \text{ Hz}$ is used to calculate the value of C_1 :

$$C_1 = \frac{1}{2\pi f_L R_1} = 3.34 \mu\text{F}.$$

One can see that reducing R_1 (for a higher and thus better microphone operating voltage) requires a larger capacitance (implying more space and cost).

Operational amplifier

The required slew rate of the amplifier can be determined by calculating the maximum rate of change at the op-amp output, arising for a sine wave at $f_{\text{max}} = 20 \text{ kHz}$ and an amplitude of $V_{\text{CC}}/2$ which sweeps the full output range. For sine waves, it can be shown⁶ that the slew rate is computed as

$$\text{SR} = 2\pi f_{\text{max}} \frac{V_{\text{CC}}}{2} = 0.188 \text{ V}/\mu\text{s}.$$

As a conservative rule, it is advised to select ten times this slew rate to eliminate any possibility of slew-induced distortion, which is very important in the analysis of audio data. This sets the required slew rate to $1.88 \text{ V}/\mu\text{s}$.

The op-amp is selected such that it adds negligible noise to the output of the amplification circuit, avoiding the degradation of the data processing. However, such low-noise operational amplifiers consume a lot of power. One thus has to analyze and compare several state-of-the-art op-amps in order to choose the one which suits the best this noise/power consumption trade-off for this application.

The related op-amp parameters that need to be well selected are the current consumption (quiescent current I_Q), the input current noise spectral density I_N and the input voltage noise spectral density E_{NV} .

The ADC voltage noise at the output is based on three noise contributions. The first noise is the thermal noise from resistors R_1 and R_2 :

$$E_{\text{NR}} = \sqrt{4 k_{\text{B}} T (R_1 // R_2)} = 6.26 \text{ nV}/\sqrt{\text{Hz}}$$

where $T = 300 \text{ K}$ is the temperature and $k_{\text{B}} = 1.38 \times 10^{-23} \text{ J/K}$ is the Boltzmann constant.

The second noise contribution is the op-amp input current noise:

$$E_{\text{NI}} = I_N (R_1 // R_2) \quad [\text{V}/\sqrt{\text{Hz}}].$$

The last noise supply is due to the op-amp input voltage noise E_{NV} .

⁶This is the highest slope of a sine function, appearing when the signal crosses 0.

The output noise spectral density, for non-correlated contributions, of the amplifier circuit is then given by

$$E_{N,ADC} = A_N \sqrt{E_{NR}^2 + E_{NI}^2 + E_{NV}^2} \quad [\text{V}/\sqrt{\text{Hz}}]$$

for which

$$A_N = 1 + \frac{R_2}{R_1} = 1602$$

is the noise gain of the op-amp (see Appendix B for details). Since the signal gain is directly determined by R_2 , it cannot be changed. On the other hand, a very low supply voltage V_{CC} decreases the value of R_1 , which increases the noise gain of the op-amp. Hence, the noise/power consumption trade-off also appears in the design of R_1 .

Finally, the RMS output noise voltage can be computed by multiplying the output noise spectral density by the square of the bandwidth of integration (spreading over an A-weighting curve). An A-weighting curve can be approximated using a 13.5 kHz noise bandwidth B_A , the RMS output noise voltage is thus (in RMS value)

$$V_{N,ADC} = \sqrt{B_A} E_{N,ADC} \quad [\text{V}].$$

This noise contribution is then brought back to the input pressure domain, the *input-referred noise* from the AFE is thus given by

$$\begin{aligned} p_{IRN,AFE} &= \frac{V_{N,ADC}}{R_2 S_{I,mic}} \\ &= \frac{\sqrt{B_A}}{R_2 S_{I,mic}} \left(1 + \frac{R_2}{R_1} \right) \sqrt{4 k_B T (R_1 // R_2) + I_N^2 (R_1 // R_2)^2 + E_{NV}^2} \quad [\text{Pa}]. \end{aligned}$$

One can directly see that this noise is roughly independent from the gain R_2 since $(1 + R_2/R_1)/R_2 \simeq 1/R_1$ in our design and the contribution from I_N is typically negligible compared to E_{NV}^2 .

Since the total input-referred noise is composed of non-correlated sources (from the microphone p_{SN} and the AFE $p_{IRN,AFE}$), their noise powers add up to give

$$p_{IRN} = \sqrt{p_{SN}^2 + p_{IRN,AFE}^2} \quad [\text{Pa}].$$

Figure 5.8 presents this input-referred noise with respect to the current consumption for several operational amplifiers. Clearly, the input-referred noise must not exceed the minimum signal sound pressure of 16 dB_{SPL}.

The ultra-low-power LMV551 op-amp has a quiescent current of only 37 µA, but the input-referred noise of 17.85 dB_{SPL} exceeds the minimum detectable input pressure. In order to keep the noise voltage not much detected from the ADC, the input-referred noise typically needs to be smaller than the minimum input signal (as depicted in Figure 5.9).

The OPA2834 has an input-referred noise of $p_{IRN,OA} = 14.22 \text{ dB}_{SPL}$ while keeping a particularly small current consumption of 170 µA. One finally selects this op-amp since it has the lowest noise in the group of three op-amps which belong to an acceptable range of quiescent current (from 100 µA to 200 µA).

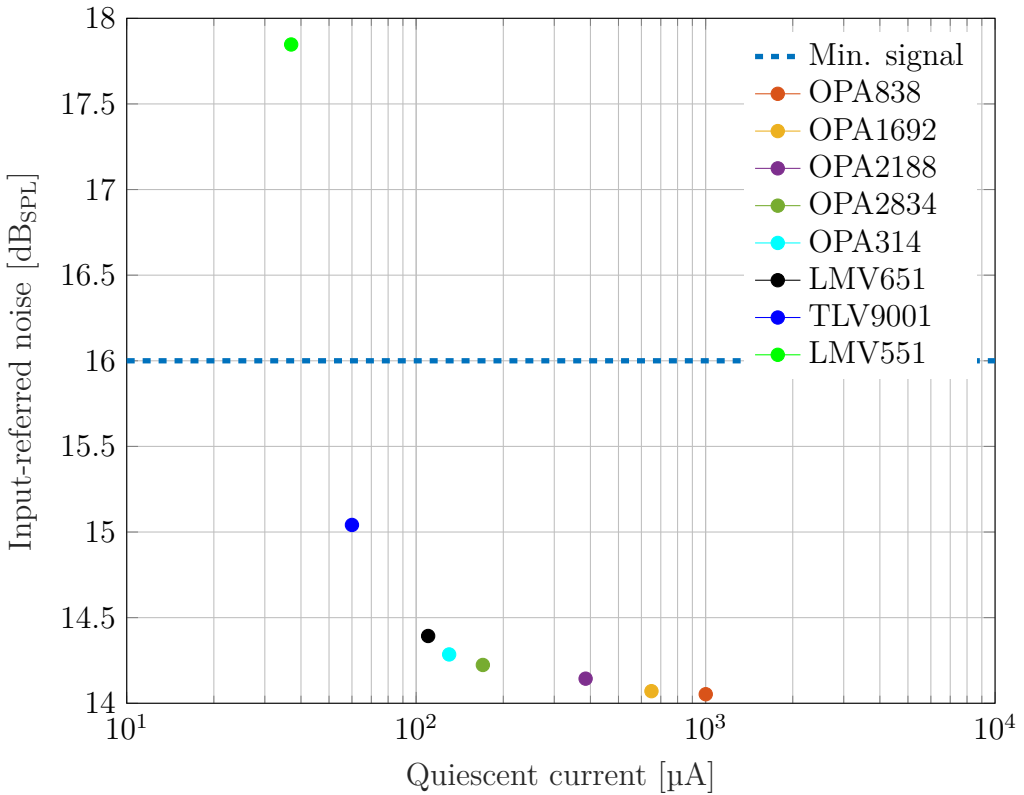


Figure 5.8: Comparison of input-referred noise and current consumption for several operational amplifiers

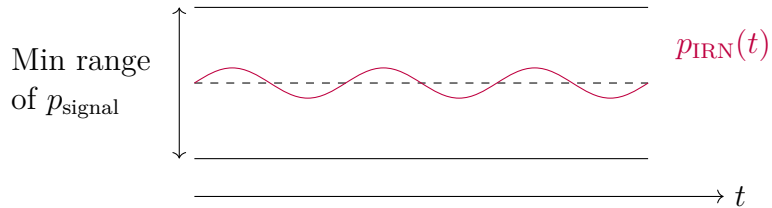


Figure 5.9: Voltage noise and resolution at the amplification output

In the end, the OPA2834 op-amp characteristics are given in Table 5.7. The slew rate of $26 \text{ V}/\mu\text{s}$ is well above the limit of $1.88 \text{ V}/\mu\text{s}$.

Criteria	Required	OPA2834	Units
Supply voltage	2.5	2.5 – 5.4	V
Quiescent current	< 200	170	μA
Input voltage noise	< 27	12	$\text{nV}/\sqrt{\text{Hz}}$
Input current noise	N/A	0.2	$\text{pA}/\sqrt{\text{Hz}}$
Slew rate	> 1.88	26	$\text{V}/\mu\text{s}$

Table 5.7: Characteristics of the selected operational amplifier: OPA2834

AFE noise voltage

The noise voltage from the AFE can be theoretically computed over an A-weighting curve of bandwidth $B_A = 13.5 \text{ kHz}$ as

$$V_{N,\text{ADC,thor}} = \sqrt{B_A} E_{N,\text{ADC}} = 2.52 \text{ mV}$$

where $E_{N,\text{ADC}}$ depends on the voltage and current noise of the OPA2834.

As a validation of the amp op selection, Figure 5.10 describes the noise voltage spectral density at the amplification output. This noise is the combination of flicker (or $1/f$) noise and thermal (flat band) noise. Hence, it depends on the frequency and is higher for frequencies below the $1/f$ corner frequency: 150 Hz for the voltage noise and 900 Hz for the current noise, as given in the op-amp datasheet. Since audio signals contain frequencies that are particularly low, the noise is sadly impinged by flicker noise. For a frequency of 22 Hz, the noise reaches $37 \mu\text{V}/\sqrt{\text{Hz}}$.

Since the noise contribution from the microphone is not represented in the simulation, this simulated noise can be compared to the theoretical value of the AFE noise (2.52 mV). Due to the frequency dependence, one needs to integrate the noise power spectral density over the whole frequency range in order to obtain the output noise voltage:

$$V_{N,\text{ADC,simu}} = \sqrt{\int_0^\infty E_{N,\text{ADC}}(f)^2 df} = 2.37 \text{ mV}.$$

As expected, the result is very similar to the theoretical one, hence not impinging the previous conclusions for the choice of the best operational amplifier.

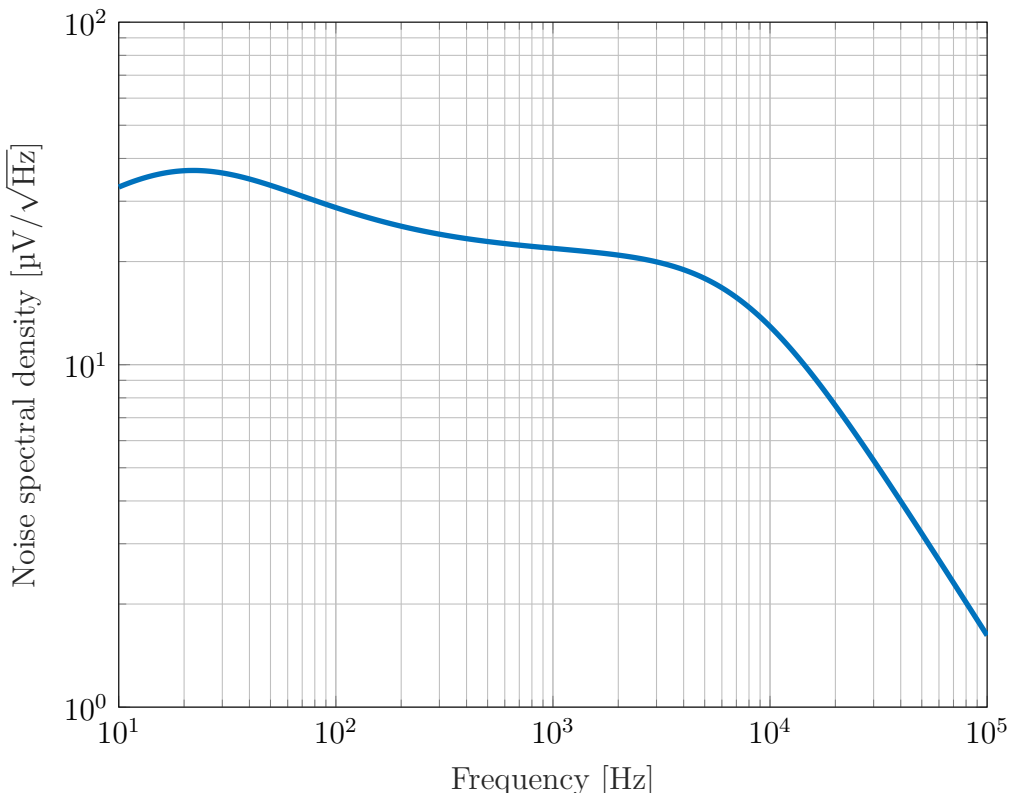


Figure 5.10: Noise voltage spectral density from AFE at the amplification output (from LTSPICE)

Total noise voltage

One can then compute the total noise voltage $V_{N,\text{tot,theor}}$ at the amplification output, resulting from the microphone noise and the AFE noise:

$$V_{N,\text{tot,theor}} = p_{\text{IRN}} R_2 S_{I,\text{mic}} = 11.2 \text{ mV}.$$

Op amp bias network

Resistors R_3 and R_4 center the op-amp input and output at the midpoint between the power supplies to allow the widest possible output signal swing. Therefore $R_3 = R_4$ for $V_B = V_{CC}/2$. The value of these resistors needs to be very high in order to limit the power supply current drawn by this voltage divider. However, the non-zero op-amp input bias current prevents the bias voltage V_B to be exactly at $V_{CC}/2$, and this variation worsens with the resistance of the bias resistors. A reasonable choice consists to set a maximum bias voltage relative variation of 0.5%:

$$\Delta V_B = \frac{1}{2} R_3 I_{b+} < 0.005 V_B \quad \Rightarrow \quad R_3 < 0.01 \frac{V_{CC}}{2I_{b+}} = 179 \text{ k}\Omega$$

where $I_{b+} = 70 \text{ nA}$ for the selected op-amp. A final value of

$$R_3 = R_4 = 150 \text{ k}\Omega$$

is finally chosen, which implies a current in the voltage divider of approximately

$$I_B = \frac{V_{CC}}{R_3 + R_4} = 8.33 \mu\text{A}.$$

This current is small (less than 5%) compared to the microphone bias current, and is a good trade-off between the power consumption and the bias voltage stability.

Capacitor C_3 is included to filter thermal noise created by the resistors and any noise which may be present on the power supply. The corner frequency of the low-pass filter is formed by R_3 , R_4 and C_3 . It should be well below the operating frequency range in order to prevent noise from affecting the audio performance of the design. A corner frequency of $f_B = 5 \text{ Hz}$ is selected:

$$C_3 = \frac{1}{2\pi f_B (R_3 // R_4)} = 424 \text{ nF}.$$

Summary

Table 5.8 summarizes the theoretical values for the amplification circuit as well as the values actually put on the experimental device depending on the available components.

	Value	
	Theoretical	Real
R_1	2.38 kΩ	2.37 kΩ
R_2	3.81 MΩ	3.83 MΩ
R_3	150 kΩ	150 kΩ
R_4	150 kΩ	150 kΩ
C_1	3.34 μF	3.3 μF
C_2	2.09 pF	2 pF
C_3	424 nF	470 nF

Table 5.8: Final values for the amplification circuit

Figure 5.11 presents the AC transfer function of the amplification circuit from the input pressure to the output voltage, which confirms a bandwidth ranging from 20 Hz to 20 kHz. The important phase variations (with additional poles) are due to the intrinsic behavior of the electret microphone.

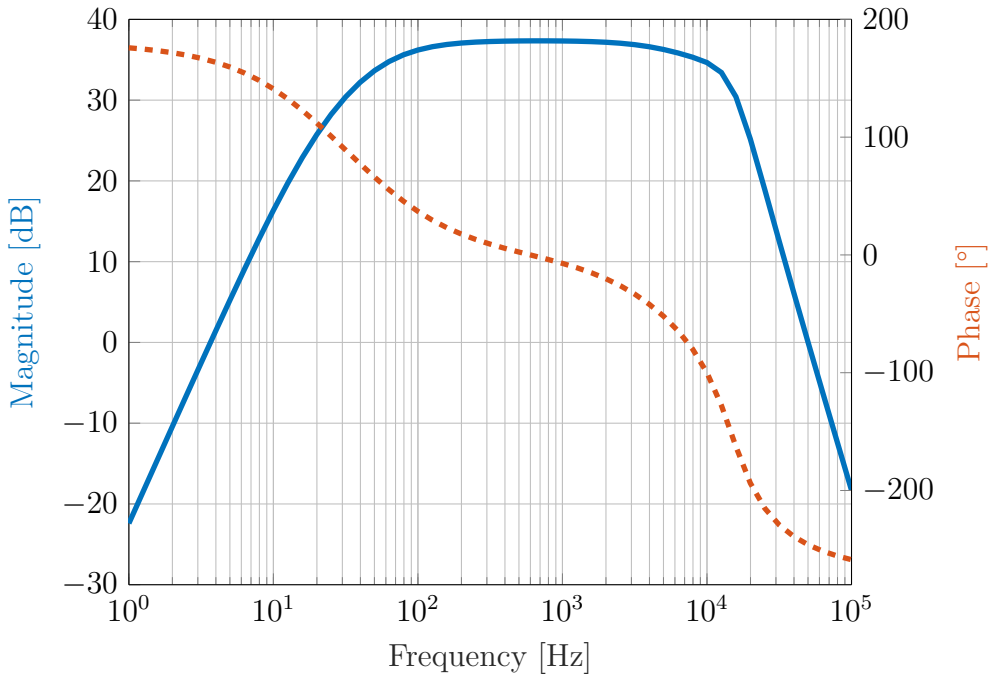


Figure 5.11: AC transfer function of the amplification circuit (from LTSPICE)

As stated before, the classical trade-off between noise and power consumption was not worth considering in the microphone selection since the other microphones suffer from too high noise. However, if the constraint on the minimum detectable sound wave were relaxed, the choice of the microphone and operational amplifier would have to be optimized conjointly by computing the input-referred noise and power consumption of the whole sensing subsystem.

Chapter 6

Data processing and transceiver

Data are processed in a microcontroller and received/transmitted in a transceiver. For this work, a CMWX1ZZABZ chip from Murata is used, which combines an STM32L072 microcontroller and an SX1276 transceiver. Its operation voltage range is 2.2 V – 3.6 V.

6.1 Microcontroller

The STM32L072 is an ultra-low-power microcontroller incorporating an Arm Cortex-M0+ 32-bit RISC core operating at a 32 MHz frequency, with embedded memories (192 Kbytes of Flash program memory, 6 Kbytes of data EEPROM and 20 Kbytes of RAM), a 12-bit ADC with hardware oversampling,... It operates from a 1.8 V to 3.6 V power supply [38].

ADC characteristics

A 12-bit analog-to-digital converter (ADC) has been used to digitize (sampling and quantization) two signals: the analog microphone voltage and supercap voltage. The resolution of an N -bit ADC is given by $V_{DD}/2^N$ where V_{DD} is the supply voltage. One might be interested to improve the ADC resolution up to 14 bits via diverse techniques (such as SAR, etc). This would allow the reading of a smaller input sound pressure (12 dB below) and make possible to process a sound pressure of 4 dB SPL (increasing the detectable distance between the sensor and the source). However, the signal quality would not benefit from this increased ADC resolution because the microphone self-noise is still 14 dB SPL.

A typical code alternates between an energy-intensive run mode (to sample sound) and a low-power sleep mode. The duty cycle between these modes will be determined in the section characterizing the power consumption (Section 7.1).

Status of supercapacitor charge

In order to know the status of the supercapacitor charge and adapt the MCU code to a possible overdischarge, the ADC reads the supercap voltage. Since this voltage is higher than the ADC supply voltage, a voltage divider is required. The supercap voltage is thus divided by two with two resistors R_{SC} of same resistance, which has to be determined according to the impedance

recommendations at the ADC input. Provided in the datasheet, the maximum input impedance for an error below 1/4 of LSB is given by (derived from the charge equation of the internal sample-and-hold capacitor)

$$R_{\text{AIN,max}} = \frac{T_S}{f_{\text{ADC}} C_{\text{ADC}} \ln(2^{N+2})} - R_{\text{ADC}} = 257 \text{ k}\Omega$$

where $T_S = 160.5$ is the number of cycles per sample, $f_{\text{ADC}} = 8 \text{ MHz}$ is the ADC clock frequency, $C_{\text{ADC}} = 8 \text{ pF}$ is the internal sample-and-hold capacitor, $N = 12$ is the number of resolution bits and $R_{\text{ADC}} = 1 \text{ k}\Omega$ is the sampling switch resistance. To increase $R_{\text{AIN,max}}$ and thus reduce power consumption, parameters such as T_S and f_{ADC} are pushed towards a low sampling frequency $f_s = f_{\text{ADC}}/T_S$ equal to 49.8 kHz in this case (the delay between each sampling being not important since the supercapacitor undergoes low variations).

Because $R_{\text{AIN,max}}$ corresponds to $R_{\text{SC}}/2$, one selects a resistance R_{SC} of $475 \text{ k}\Omega$. This value produces a negligible current consumption of

$$I_{\text{SC,ADC}} = \frac{V_{\text{SC}}}{2R_{\text{SC}}} = 4.7 \mu\text{A}$$

in the worst-case scenario when the supercapacitor is fully charged at 4.5 V .

Finally, the ADC input leakage current provided in the datasheet is maximum $I_{\text{in,ADC}} = 50 \text{ nA}$. The ADC voltage due to the non-zero input current is thus $(V_{\text{SC}} - R_{\text{SC}} I_{\text{in,ADC}})/2$ instead of $V_{\text{SC}}/2$, leading to a maximum relative error of

$$E_{\text{rel}} = \frac{R_{\text{SC}} I_{\text{in,ADC}}}{V_{\text{SC}}} = 0.85 \%$$

in the worst-case scenario when the supercapacitor is fully discharged (2.8 V). This error is negligible.

6.2 Transceiver

The SX1276 transceiver features a LoRa long-range modem that provides ultra-long range spread spectrum communication [39]. LoRa has been increasingly used in the IoT domain thanks to their compromise between range, interference immunity and energy consumption [40]. The transceiver chip is connected to an external ISM (industrial, scientific and medical purposes) antenna in the range $790 \text{ MHz} - 960 \text{ MHz}$.

The receiver is used for over-the-air (OTA) updates and thus implies that the MCU has reconfiguration capabilities to keep up with application, security and communication protocol updates. During such updates, the challenge is the instantaneous power consumption when the wireless radio is in receive mode and the microcontroller is reprogramming its internal Flash memory (recall that the maximum current consumption at the PMU output is 80 mA and that the energy storage is very limited). To lower this peak power, a smart decomposition of the firmware packets is required.

The transmitter is used to send data to a gateway, mainly information about the analyzed input sound pressure and hence bird species. All data are handled in the RAM memory of the MCU,

but important data that need to be transmitted are stored in the FLASH memory in order to prevent them from being erased after an unexpected shutdown.

The radio-frequency communication for this smart sensor, including power consumption and security in LoRaWAN networks, has been carefully discussed and optimized in a concurrent master thesis [41].

Chapter 7

Power supply

In this chapter, the total current consumption is evaluated. The solar cells and supercapacitor are then sized accordingly.

7.1 Power consumption

The power consumption will be computed separately for each block. Since the voltage regulator inside the PMU is an LDO, the current drawn in the circuit is the same as the current drawn in the supercapacitor. For each subsystem, it thus makes sense to provide the current consumption I instead of the power consumption since the latter is higher from the supercap point of view ($V_{SC} I$) than from the subsystem point of view ($V_{DD} I$).

Sensing

As seen in Figure 5.5, the current consumption from the sensing subsystem is composed of

- the current through the microphone branch (with R_1): $I_{mic} = 358 \mu A$ (see Table 5.5),
- the op-amp quiescent current: $I_Q = 170 \mu A$,
- and the current through the voltage divider with R_3 and R_4 to bias the op-amp: $I_B = 8.33 \mu A$.

This leads to a current consumption of $I_{sensing} = 536 \mu A$.

Power Management

The current consumption of the power management subsystem is composed of

- the leakage current of the supercapacitor: typically $I_{Q,SC} = 500 \mu A$ (will be refined in Section 7.3),
- the voltage divider to read the supercap voltage at the ADC input $I_{SC,ADC} = 4.7 \mu A$,
- and the PMU quiescent current: $I_{Q,PMU} = 0.6 \mu A$.

This leads to a current consumption of $I_{power} = 505 \mu A$.

Data processing and transceiver

For this part, it is possible to adapt the code in the microcontroller to match the best capabilities of the system. In view of the power consumption from the previous parts and the typical harvested power from solar cells, one will aim to keep the MCU/RF consumption below 4 mA.

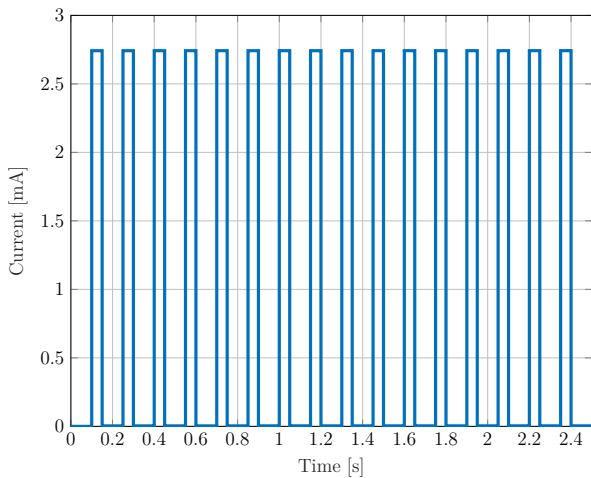
First case without transceiver

As a first approximation, a run mode that only processes data is considered (that is, without transmission or reception). A typical scheme for this application is to alternate a run mode and standby mode.

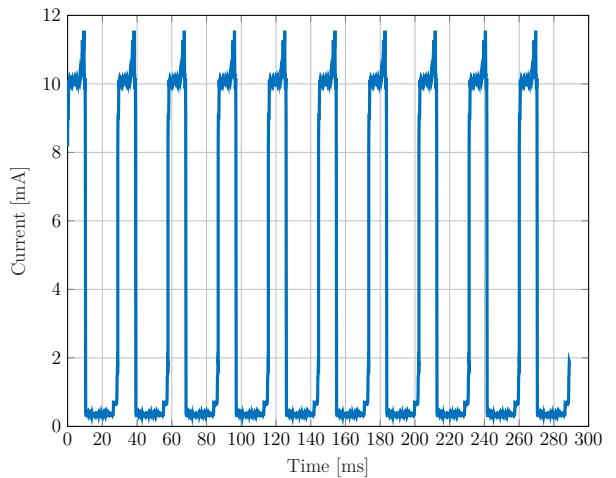
Addressing a simple scheme allows using a simulation tool (Wisebatt) in order to estimate the power consumption. As seen in Figure 7.1a, Wisebatt estimates the run mode at 2.74 mA and the standby mode at 3.64 μ A. With a duty cycle of 1/3, one obtains an average current consumption of

$$i_{\text{avg}} = \frac{1}{3} 2.74 \text{ mA} + \frac{2}{3} 3.64 \mu\text{A} = 0.913 \text{ mA.}$$

By assuming that it takes 50 ms to sample and process the data, it leads to a cycle duration of 150 ms. However, the simulation tool misses the FFT operation that is achieved inside the microcontroller, which significantly reduces the current consumption in run mode. To refine this poor model, experimental measurements of the current consumption have been achieved (see Figure 7.1b). With a duty cycle of 1/3, they show an average current consumption of 3.88 mA since the run mode consumes 10.1 mA. An MCU current consumption of 3.88 mA will be kept as reference for designing further components, it allows keeping a precise track of the input sound wave (one third of the time at high run/sleep cycle frequency) with sufficiently low power consumption. It is worth noting that the increase in current consumption before each sleep mode is due to the microcontroller which saves the data by writing in its registers (and write operations consume more than the read operations appearing at the beginning of each run mode).



(a) Wisebatt simulation



(b) Experimental results

Figure 7.1: Current consumption of the CMWX1ZZABZ without TX/RX

Second case with transceiver

Now, one considers the power consumption related to the transceiver part. First, Figure 7.2 shows the current consumption for sending one packet of 51 bytes, with a peak current of 49.5 mA for 130 ms. One verifies that this peak current never exceeds the maximum output current of 80 mA from the PMU (see Table 4.1).

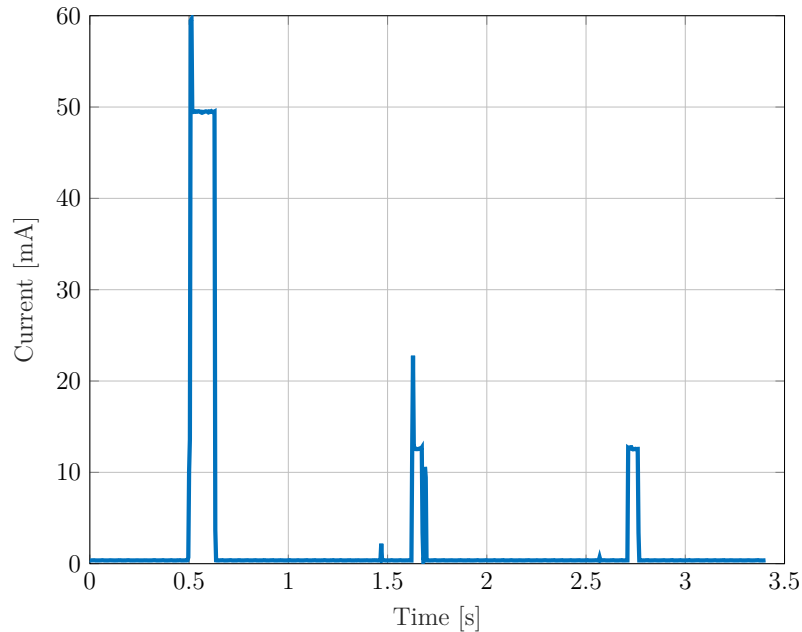
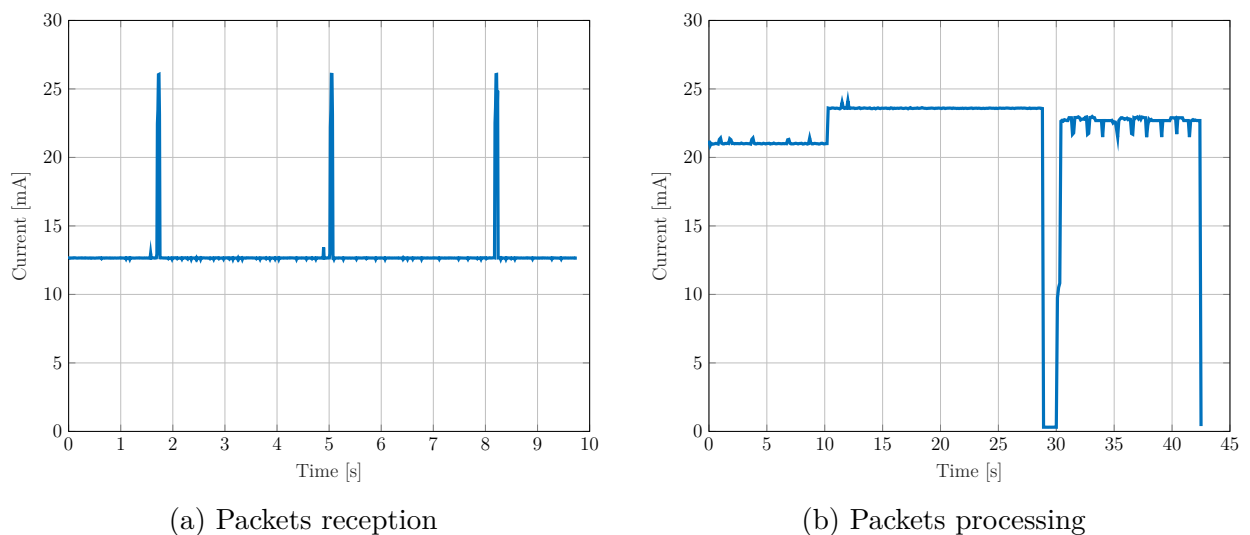


Figure 7.2: Current consumption for sending one packet of 51 bytes

Second, data reception is characterized through an over-the-air firmware update (FUOTA). Figures 7.3 show the current consumption of a typical FUOTA.



(a) Packets reception

(b) Packets processing

Figure 7.3: Current consumption for a FUOTA

The first figure corresponds to the packet reception (in Class-C¹) with a constant current of 12 mA. Only a part of the consumption is shown, it has a periodic profile during 259 s.

The second figure is related to the packet processing of the FUOTA, composed of three steps: hash computation of the received fragment to ensure its validity (i.e. no data corruption during the transmission), computation of the reverse delta (i.e. the firmware that has changed), and computation of the new firmware image based on the previous image and the delta.

Receiving and processing the packets consume 14.1 mA on average for 301 s, that is an energy of 10.6 J. Since the update period is flexible, it is achieved when the device does not process audio data (i.e. during the night). Provided that the sensor is able to sustain the amount of energy as well as the maximum power, over-the-air updates (which are less common) are not taken into account in the power budget hereafter.

Total power consumption

Table 7.1 summarizes the power budget for the whole system. As expected, the most energy-intensive part is the microcontroller and radio-frequency subsystem.

	Current [mA]
Data processing	3.88
Power management	0.50
Sensing	0.54
Total	4.92

Table 7.1: Description of the theoretical power consumption in the system

Depending on the supercapacitor voltage, the total power consumption finally varies linearly between 13.8 mW (at 2.8 V) and 22.1 mW (at 4.5 V) according to $P_{\text{tot}} = V_{\text{SC}} I_{\text{tot}}$.

7.2 Solar cells

Solar cells are electrical devices that convert the energy of light into electricity by the photovoltaic effect. The current generated by such cells is decreasing with the voltage. It leads to a maximum of the harvested power (see Figure 7.4), which is called the MPP (for Maximum Power Point).

The main figures of merit for solar cells are thus the current and voltage at the maximum power point, as well as the surface area since the goal is to maximize the harvested power per unit area and thus minimize the area on the PCB. It is worth noting that the current and power are provided at one sun (1 mW/mm²), and the power is the electric power generated by the solar cells.

¹Class-C endpoints use the most power but have the shortest latency.

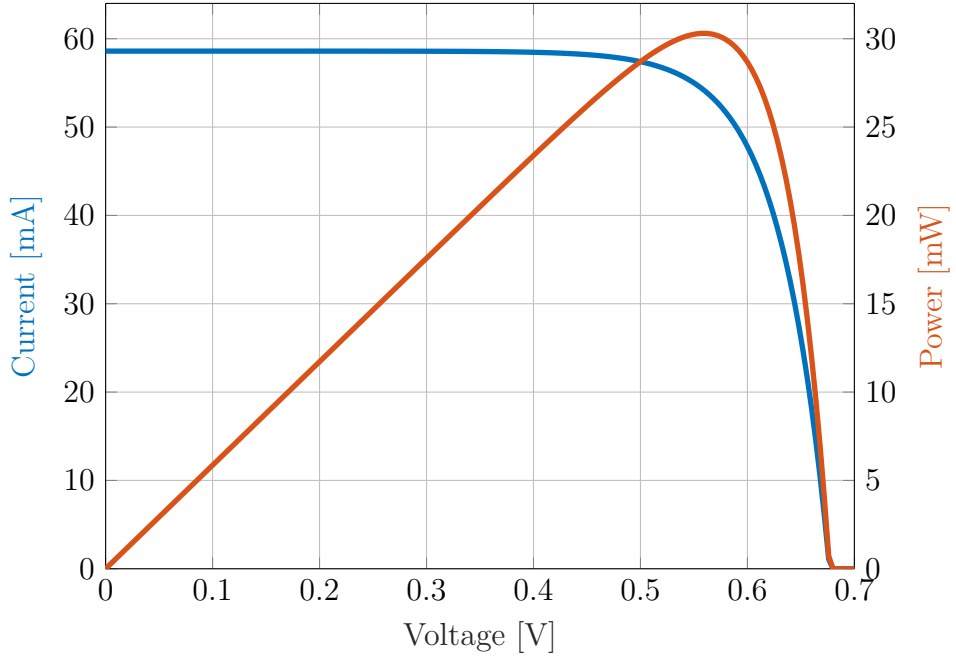


Figure 7.4: IV and PV curves of a typical solar cell: SM141K06L

A great advantage of solar cells is their ability to combine them easily in series (doubling the voltage) or in parallel (doubling the current), provided that the total voltage does not exceed the voltage limit of 5 V of the power management unit. Based on the comparison depicted in Table 7.2 between three cells of different sizes, the SM141K06L model is selected for its high power per unit area of 0.1905 mW/mm^2 . Alternatively, this electric power per unit area can be validated by computing the product between the sun intensity and the efficiency of the solar cells (approximated to 25% in the datasheet compared to 19.05% computed here).

	KXOB25-14X1F	SM141K06L	SLMD481H08L
Current [mA]	55	55.1	178
MPP Voltage [V]	0.56	3.35	4
Power [mW]	30.7	184	714
Surface [mm x mm]	23×8	42×23	89×55
Power per unit area [mW/mm ²]	0.1668	0.1905	0.1459

Table 7.2: Comparison of several solar cells

This model is a set of six single solar cells in series, raising the MPP voltage from 0.56 V to 3.35 V. Figure 7.4 provides the IV/PV curves for one of the single cells.

Now that the cell with the best power per unit area is selected, the following of this section is dedicated to the computation of the required number of such cells in order to daily provide enough energy to the whole circuit via the supercapacitor. For this purpose, a model of the harvested energy from the sun is required.

Illuminance

The luminosity profile over a whole day needs to be measured in order to estimate the harvested solar energy. For this purpose, a light meter (model *testo 540*) has been used². It is a precise light sensor but the measurement is only shown on a screen, preventing the user to continuously record the data over a whole day. Figure 7.5 thus presents the measurements made at regular intervals in a shady place of Louvain-la-Neuve (to replicate a place similar to a forest). The weather was cloudy, which gives an illuminance very near the worst-case scenario and hence allows the solar cells to be selected based on the darkest days.

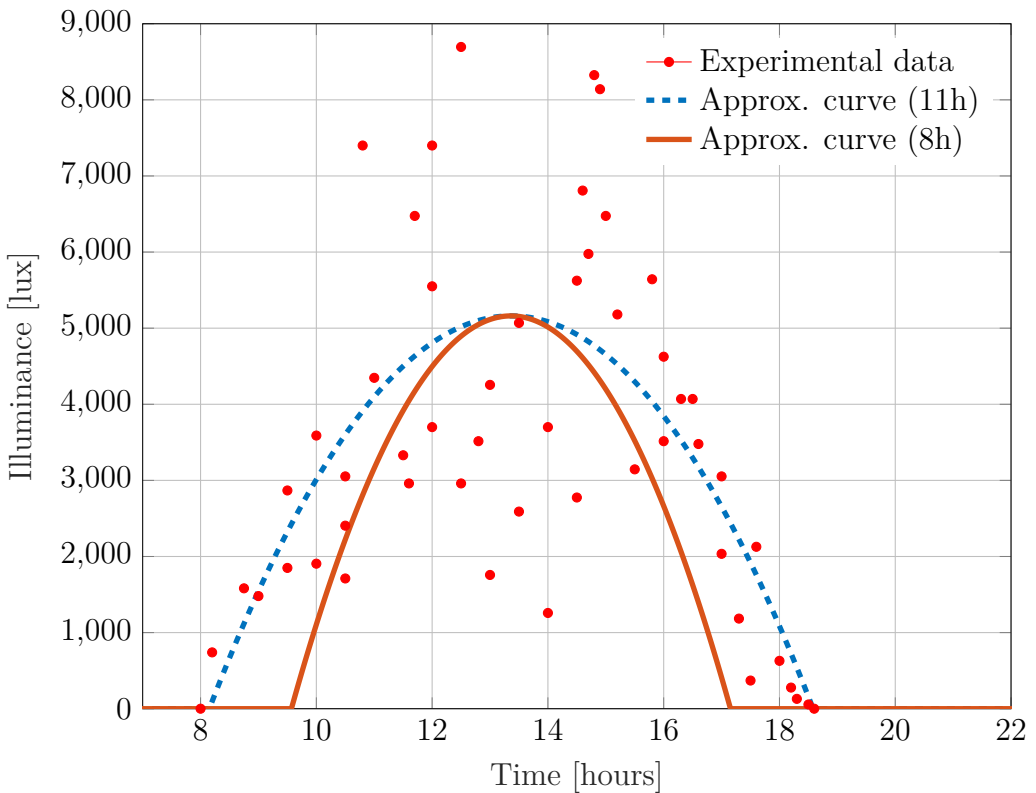


Figure 7.5: Daily luminosity (Louvain-la-Neuve, from March 3 to March 6, 2020)

These data are extremely variable, mainly due to the motion of clouds. A polynomial regression of second order $L(t)$ allows better representing the trend over a day (in dashed blue).

The data have been taken during days with 11 hours of sunlight (averaged between March 3 and March 6, 2020) while the sensor has to work under smaller periods of sunlight (down to eight hours in the winter [42]). Assuming that the daily harvested energy is proportional to the duration of sunlight, the following computations will be done accordingly by horizontally shrinking the graph by 8/11 (in red).

More rigorously, one should also shrink the graph vertically since the sunlight is weaker in winter. Indeed, the same incoming sunlight is distributed over a larger area at higher latitudes (see Figure 7.6). However, scaling the device to the very worst-case scenario (less than 10% of

²Smartphone applications such as *Physics Toolbox* also exist but provide imprecise results.

the year) is not advisable since it would imply significant overscaling (of the solar cells and supercapacitor). Consequently, the microcontroller algorithms will be less resource-intensive during the winter in order to match the specifications of energy harvesting and storage, which is coherent with the fact that fewer birds are active during this period.

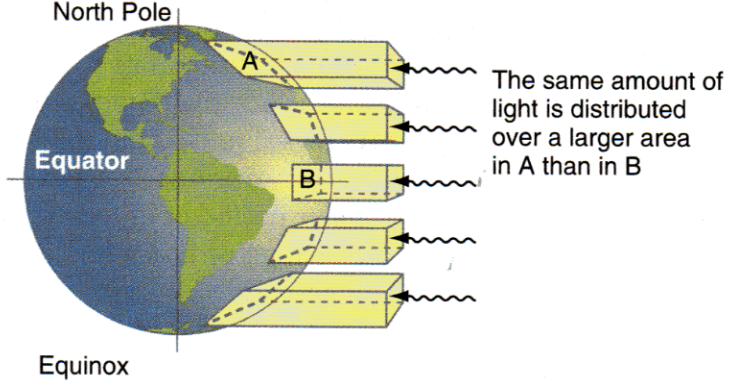


Figure 7.6: Sunlight towards Earth at the equinox [43]

Power conversion

From this solar energy, solar cells generate a current which is proportional to the illuminance. Most of the solar cell datasheets provide an IV curve at a fixed illuminance of $1\text{ sun} = 1 \times 10^3 \text{ W/m}^2$. Since $1\text{ lux} = 0.0079 \text{ W/m}^2$ for the solar spectrum, the harvested current $I_{\text{cell}}(t)$ from one solar cell is given by

$$\frac{I_{\text{cell}}(t)}{L_{\text{sun}}(t)} = \frac{I_{1\text{sun}}}{1} \quad \Rightarrow \quad I_{\text{cell}}(t) = I_{1\text{sun}} L_{\text{sun}}(t) = 0.0079 \times 10^{-3} I_{1\text{sun}} L(t) \quad [\text{A}]$$

where $L(t)$ and $L_{\text{sun}}(t)$ are the instantaneous illuminance (resp. expressed in lux and sun) and $I_{1\text{sun}}$ is the current generated at the MPP under 1 sun (provided in the datasheet).

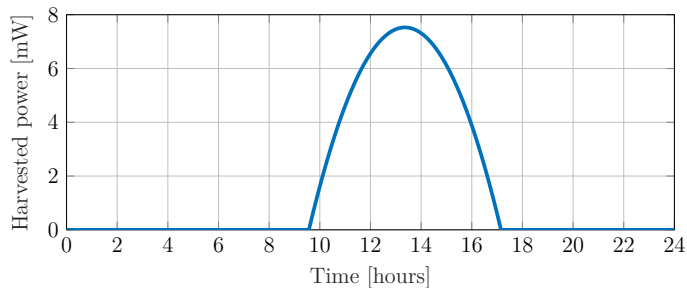


Figure 7.7: Daily view of the harvested power with SM141K06L solar cells

For the selected solar cells, Figure 7.7 gives the harvested power throughout the day³:

$$P_{\text{cell}}(t) = I_{\text{cell}}(t) V_{\text{cell}} = 0.0079 \times 10^{-3} I_{1\text{sun}} V_{\text{cell}} L(t) \quad [\text{W}]$$

with $V_{\text{cell}} = 3.35 \text{ V}$ and $I_{1\text{sun}} = 55.1 \text{ mA}$.

³As mentioned previously, notice that the graph is shrunk such that the day benefits from sunlight during only eight hours.

Charge of the supercapacitor

The next paragraphs will discuss how the power management unit transforms the input and output powers with two different voltage regulators.

The input power charging the supercapacitor from the solar cells is independent from the supercapacitor voltage. Indeed, the voltage at the maximum power point is converted to the supercap voltage through a boost converter with efficiency $\eta_{\text{boost,PMU}} = 92\%$ derived in Section 4.2. The input power is thus

$$P_{\text{in,solar}}(t) = n_{\text{cell}} I_{\text{cell}}(t) V_{\text{cell}} = \frac{1}{\eta_{\text{boost,PMU}}} I_{\text{in,SC}}(t) V_{\text{SC}}(t) \quad [\text{W}]$$

where n_{cell} is the number of solar cells required for the device, $I_{\text{in,SC}}(t)$ is the input current through the supercapacitor and $V_{\text{SC}}(t)$ is the voltage across the supercapacitor.

Regarding the power consumption, the PMU converts the supercapacitor voltage to a constant voltage $V_{\text{CC}} = 2.5 \text{ V}$ via a low-dropout (LDO) regulator. Neglecting the quiescent current, LDOs keep the same current while the voltage is reduced. The output power is thus reduced, this is why it is important to maintain a small dropout (voltage difference between the input and output). Hence, the output current is independent from the supercapacitor voltage and not the output power since the ratio of output power fed to the circuit over the output power actually retrieved from the supercapacitor is given by

$$\frac{P_{\text{out,circuit}}}{P_{\text{out,SC}}} = \frac{I_{\text{out}} V_{\text{CC}}}{I_{\text{out}} V_{\text{SC}}} = \frac{V_{\text{CC}}}{V_{\text{SC}}}.$$

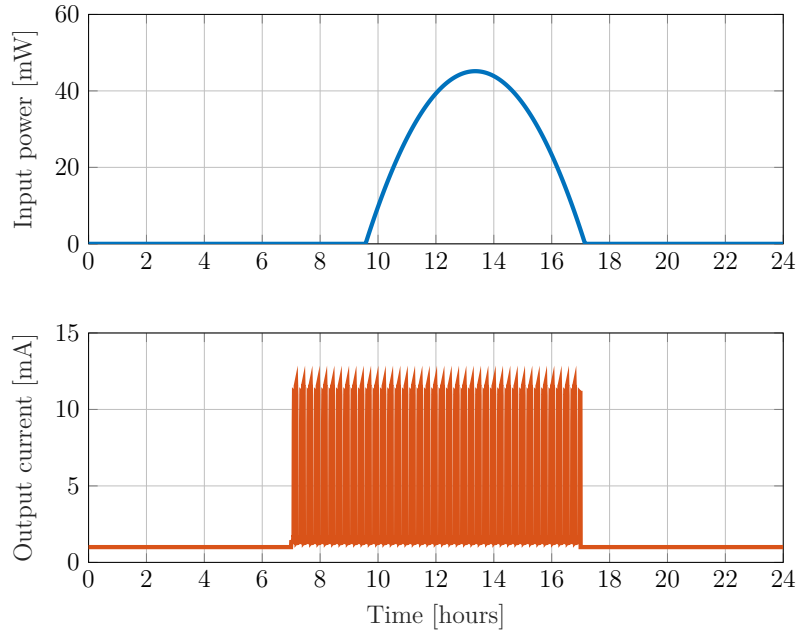


Figure 7.8: Input power and output current for six solar cells and a typical profile of cyclic consumption

In the end, Figure 7.8 depicts the input and output variables which are independent from the supercapacitor voltage: the input power and the output current. These are thus the only

quantities which can be plotted without measuring the supercapacitor voltage. The input power is given with six solar cells. One verifies that it never reaches the maximum PMU input power of 550 mW (see Table 4.1).

The output current has the cyclic profile from the MCU analyzed in Figure 7.1b on which a current consumption of 1.04 mA has been added for the remaining of the system (as computed in Table 7.1). Since the following components are designed for the worst-case scenario, the input power is not sufficient to maintain the microcontroller in operation at night. It is thus limited to a typical time window of bird activity (from 7 h to 17 h). When days have longer sunlight time, the device will receive more energy and thus either support longer processing periods (up to 24 h per day) or allow more frequent radio-frequency communication (for both data transmission and firmware update).

First-order non-linear differential equation for the supercapacitor voltage

Having two different physical quantities (the power and the current) conserved when the supercapacitor voltage changes leads to slightly more complicated computations of the supercapacitor voltage over one day⁴. The rigorous approach consists to write the equation for the charge of a capacitor:

$$\begin{aligned}\frac{dV_{SC}}{dt} &= \frac{1}{C} (I_{in,SC}(t) - I_{out,SC}(t)) \\ &= \frac{1}{C} \left(\eta_{boost,PMU} \frac{P_{in,solar}(t)}{V_{SC}(t)} - I_{out,SC}(t) \right) \\ &= \frac{1}{C} \left(\eta_{boost,PMU} n_{cell} I_{cell}(t) \frac{V_{cell}}{V_{SC}(t)} - I_{out,SC}(t) \right)\end{aligned}$$

which is a non-linear first-order differential equation for the variable $V_{SC}(t)$. Nonetheless, one can notice that the equation is written as

$$\frac{dV_{SC}}{dt} = f(V_{SC}, t)$$

where $f(V_{SC}, t)$ is a function of V_{SC} and t . It can thus be easily solved numerically for example via the forward Euler method:

$$\begin{aligned}V_{SC}(t + dt) &= V_{SC}(t) + dt f(V_{SC}(t), t) \\ &= V_{SC}(t) + \frac{dt}{C} \left(\eta_{boost,PMU} n_{cell} I_{cell}(t) \frac{V_{cell}}{V_{SC}(t)} - I_{out,SC}(t) \right).\end{aligned}$$

⁴Having the input and output currents independent from the supercapacitor voltage would lead to the simple equation:

$$V_{SC}(t) = V_{SC}(t_0) + \frac{1}{C} \int_{t_0}^t (I_{in,SC}(t) - I_{out,SC}(t)) dt.$$

Likewise, having the input and output powers independent from the supercapacitor voltage would lead to the equation:

$$E_{SC}(t) = E_{SC}(t_0) + \int_{t_0}^t (P_{in,SC}(t) - P_{out,SC}(t)) dt$$

where $E_{SC} = CV_{SC}^2/2$ to obtain the voltage.

starting with $V_{SC}(t_0) = V_{CC} + 0.3 = 2.8 \text{ V}$ which is the minimum voltage across the supercapacitor due to a minimum dropout of 0.3 V . The value t_0 is thus the time for which the supercapacitor begins to charge, in other words, when the input power starts to exceed the output power: $\eta_{\text{boost,PMU}} n_{\text{cell}} I_{\text{cell}}(t_0) V_{\text{cell}} = I_{\text{out}}(t_0) V_{\text{SC}}(t_0)$.

Finally, Figure 7.9 depicts the numerical solution of the supercapacitor voltage throughout the day for three different numbers of cells. At night, the voltage is linearly decreasing due to the stable current consumption of the sensing and power subsystems. When the microcontroller is activated in the morning, a wavy and amplified diminution appears until the sun provides enough energy to recharge the supercap voltage in the middle of the day. One can see the small ripple due to the sharp transitions of the consumed current when the microcontroller alternates between run and sleep mode.

The number of cells is chosen to come back to the minimum voltage after one day (close the loop). If there are not enough cells, the voltage will fall below this minimal voltage and the circuit will be shut down during a few hours. If there are too many cells, the voltage will be higher day after day, which is useless and not efficient due to the preference of low dropout when using LDO. The maximum input power of the PMU could also be reached during peak sun illuminance, which will break the component. The optimal number of cells is thus six, as the red curve in Figure 7.9 is perfectly suited for the current consumption.

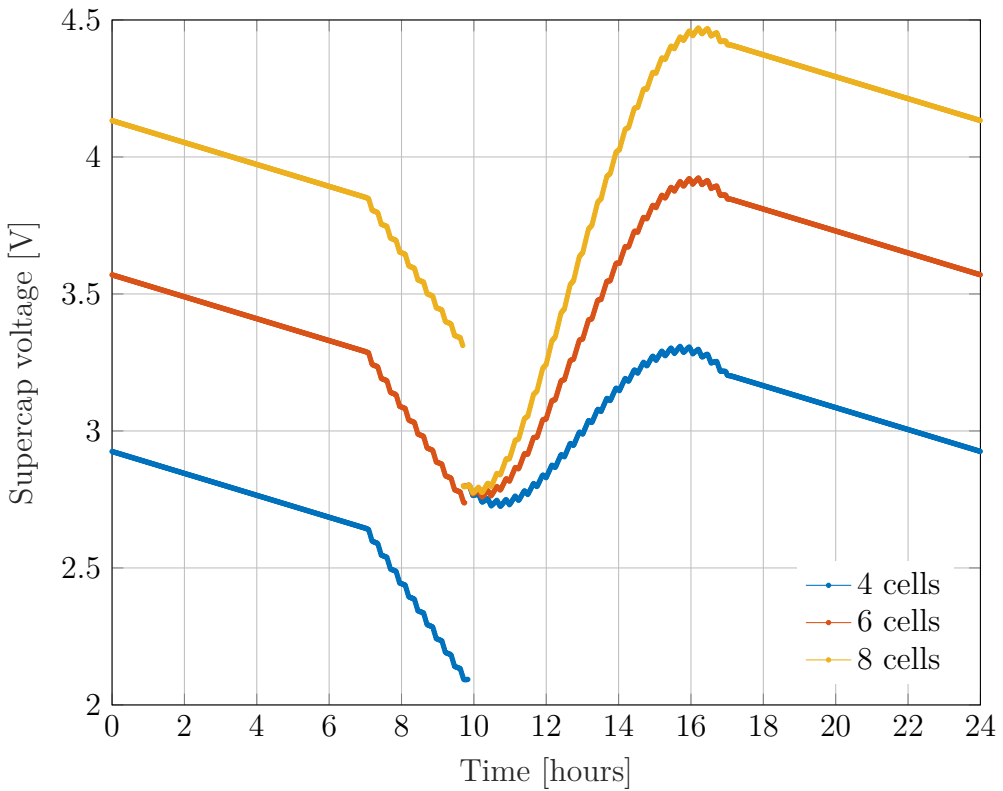


Figure 7.9: Voltage across the supercapacitor for three numbers of cells

7.3 Supercapacitor sizing

Although the size of the supercapacitor appears inside the charge equation in the previous computations, its impact is small compared to the impact of the number of solar cells. This small impact comes from the charge equation stating that C changes the slope of $V_{SC}(t)$ (applying only a vertical stretching of the curve). This increase in supercap voltage induces a higher dropout in the output voltage conversion, decreasing the efficiency of the regulation. It is then required to size the supercapacitor such that the maximum voltage set by the PMU (4.5 V) is never exceeded.

Figure 7.10 provides the simulation results for three different capacitances. One can first see that the maximal voltage is reached for $C = 50 F$ but it fails to be active during one day since the voltage drops below the 2.8 V (its operation near the maximum voltage produces many power losses in the LDO), the minimum capacitance for this work is thus between 50 F and 100 F.

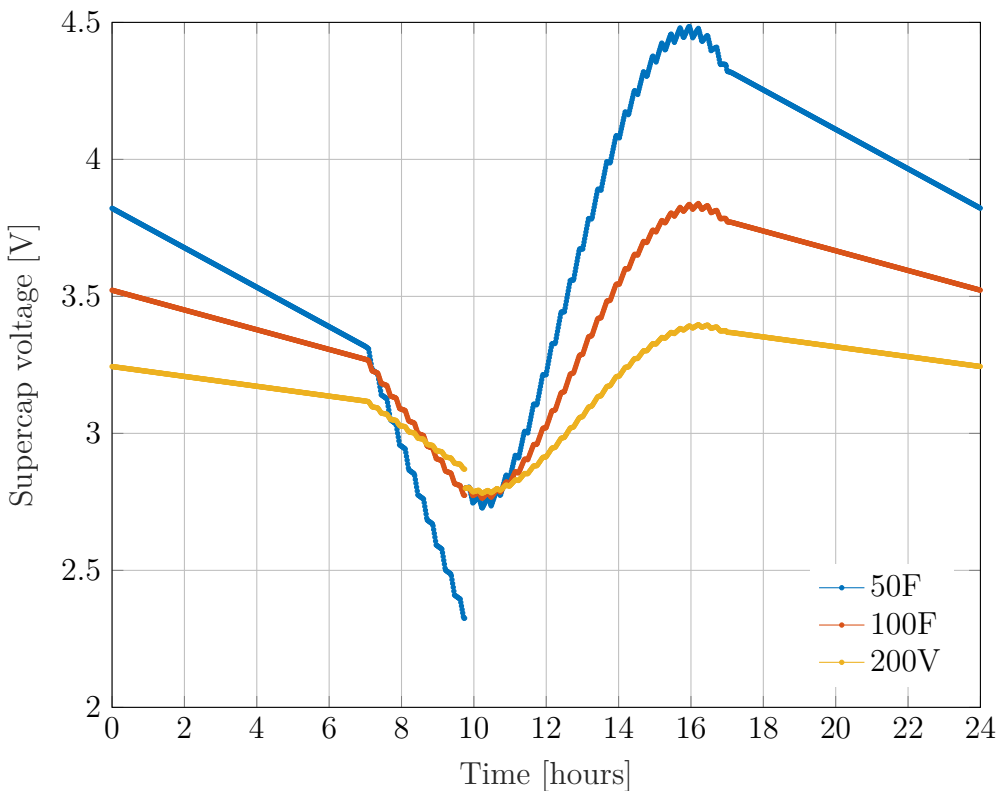


Figure 7.10: Voltage across the supercapacitor for three different capacitances

A common (and possibly the only one in Europe) manufacturer for such high capacitances is Vishay, it has a broad range of supercapacitors from 4 F to 90 F and from 1.8 V to 8.4 V. The minimal voltage matching the specifications of this work is 4.2 V since the operating voltage range must lie inside the PMU range (2.8 V to 4.5 V). Table 7.3 provides a comparison between the two best solutions: a supercapacitor of 90 F and a set of four supercapacitors of 15 F.

	MAL219690101E3	MAL219691213E3 ($\times 4$)
Capacitance [F]	90	$15 \times 4 = 60$
Rated voltage [V]	4.2	4.2
Leakage current [μA]	500	$120 \times 4 = 480$
Volume [mm x mm x mm]	$35 \times 26.5 \times 15$	$(14 \times 10 \times 12) \times 4$
Cost [\$]	19.16	$8.93 \times 4 = 35.72$

Table 7.3: Comparison of several supercapacitors

As shown in Figure 7.11, these typical supercapacitors present a linear discharge under constant current only locally in a range between 4.4 V and 5.4 V (for a 5.6 V supercapacitor). Below 4.4 V, the supercap voltage drops very fast and falls below its operation voltage. Selecting a capacitance of 5.6 V would thus not allow the PMU, limited to 4.5 V, to charge the supercap in its operating voltage range. Even if it is below the 4.5 V of the PMU, a 4.2 V supercapacitor is thus required to work in the range where most of the energy is actually stored (between 3.1 V and 4 V). One can finally notice that the leakage current is not negligible, making this type of supercap unsuited for ultra-low-power devices (sub-mW total power consumption).

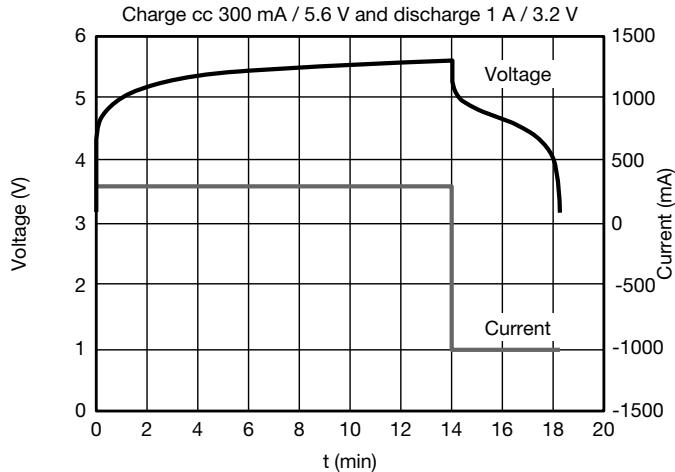


Figure 7.11: Constant current charge and discharge: 90 F / 5.6 V [23]

The all-in-one supercapacitor of 90 F is selected because its capacitance is 50% higher and its cost is lower with not much additional leakage current and space on the board. It thus allows more power consumption (namely processing in the microcontroller) during periods of higher sunlight without saturating the supercapacitor voltage. Based on Figure 7.10, it is expected that the voltage follows the red curve and thus reaches a peak at 3.8 V.

Figure 7.12 gives the voltage split for a 90 F / 4.2 V supercap, which perfectly fits into the PMU and supply specifications.

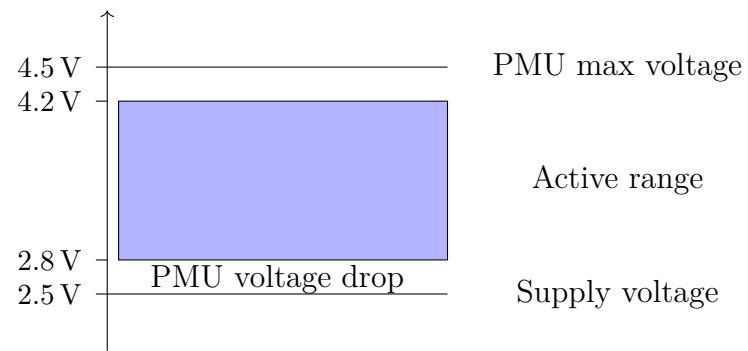


Figure 7.12: Voltage split for a 90 F / 4.2 V supercap coupled with the AEM10941

Chapter 8

Final model

8.1 Description

Figure 8.1 presents the electronics diagram of the final model, it summarizes all the blocks previously analyzed and characterized.

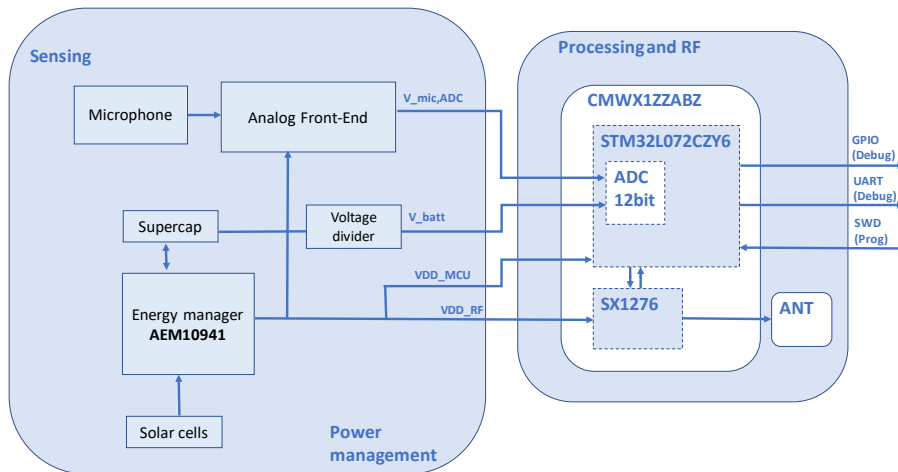


Figure 8.1: Electronics diagram of the final model

The final model is a stack of two boards: a board for data processing and radio frequency on top of a board for sensing and power management.

8.2 Design

The design of the final model is given in Figure 8.2. One can see the six solar cells, the supercapacitor in blue, the microphone in light gray, as well as five headers for current/voltage

measurements. The components are placed such that the solar cells receive the maximum of sunlight.

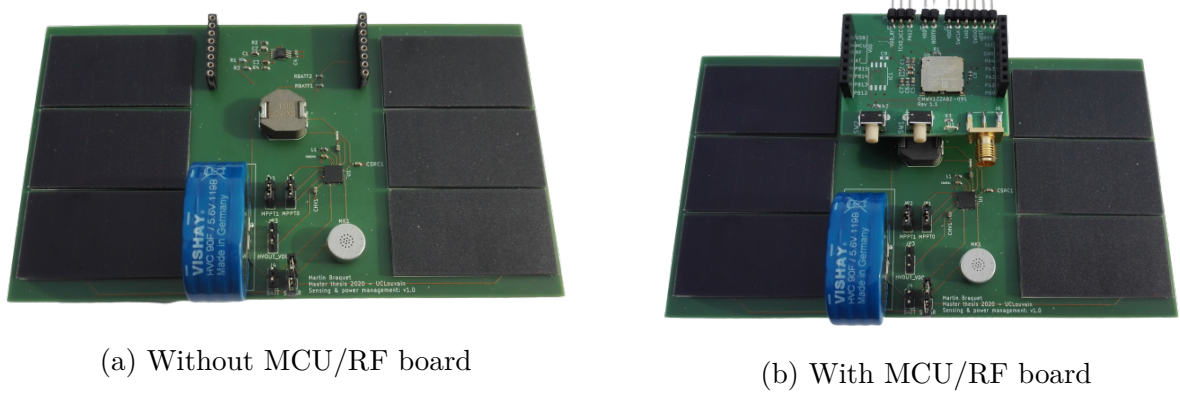


Figure 8.2: Pictures of the final model

Prototyping

The PCB schematic and layout are available in Appendix C.

8.3 Validation

This section describes the experimental results obtained with the real device.

Power consumption

The current consumption measured in the different parts is given in Table 8.1. These measurements have been made with a Source Measure Unit: Keithley 2400 [44].

Current [μA]	
Supercap leakage	95
Sensing	904
PMU	50
MCU	470
Total	1645

Table 8.1: Description of the current consumption in the system

When the supercapacitor is fully disconnected, a leakage current of $95 \mu\text{A}$ is noticed, which is indeed below the maximum value of $500 \mu\text{A}$ in the datasheet.

In the AFE, the microphone consumes $380 \mu\text{A}$. The op-amp consumes $524 \mu\text{A}$, which is more than expected since it has two channels. One should have chosen an op-amp with only one channel.

As given in the datasheet, the PMU quiescent current is less than $60\ \mu\text{A}$ ($50\ \mu\text{A}$).

The current consumption for a basic code in the MCU (FFT operations without RF and duty cycle run/deepsleep mode of 10%) is $470\ \mu\text{A}$, corresponding to a run mode consuming $4.7\ \text{mA}$. It is approximately the result obtained in the theoretical section.

Solar cells

Table 8.2 compares the harvested power from the solar cells in function of the MMP ratio under a fixed interior lighting. The voltage is fixed by the SMU while it measures the current. The highest power is achieved at 70% of the open-circuit voltage (4.15 V), which is selected in hardware via a header connected to the PMU. For low supercap voltage (below 3.3 V), this 2.9 V MPPT voltage will not lead to the best PMU efficiency since it exceeds the 2.4 V derived in Section 4.2, but the gain in solar power at this MPP compensates for the loss of efficiency.

MPP ratio	Voltage [V]	Current [mA]	Power [mW]
70%	2.9	20.2	58.6
75%	3.11	17.9	55.7
85%	3.53	11.1	39.1
90%	3.73	3.5	13.1

Table 8.2: Harvested power from the solar cells in function of the MMP ratio

Table 8.3 gives the harvested current under different lighting from the solar cells at the MMP voltage (2.9 V). Since the data were taken at noon, they show more harvesting energy than for the theoretical analysis (see Figure 7.5).

	Current [mA]
In the shade	30
Cloudy	50
Sunny	105

Table 8.3: Harvested current under different lighting from the solar cells at the MMP voltage

Supercapacitor

Figure 8.3 needs to be compared to Figure 7.11, it provides the supercapacitor discharge under a constant current of $500\ \text{mA}$ after being charged to its maximum voltage (4.2 V) and kept at this voltage for 30 minutes (as recommended in the datasheet). It can be noted that the voltage is around 3.1 V for the most important part of the operation, which is beneficial since the LDO in the PMU has a low dropout in this case (and thus a good efficiency). Additionally, the supercapacitor is not in operation under 2.5 V, which proves that the best type of DC-DC converter for this application is an LDO (and not a buck-boost converter which would allow stepping up the voltage as well). The total energy stored in this $90\ \text{F}/4.2\ \text{V}$ supercapacitor is

computed as

$$E_{\text{SC}} = \int_0^{\infty} P_{\text{SC}}(t) dt = I_{\text{discharge}} \int_0^{\infty} V_{\text{SC}}(t) dt = 851.6 \text{ J}$$

and is slightly different from the usual equation describing the energy in a capacitor: $E_{\text{cap}} = CV^2/2 = 793.8 \text{ J}$.

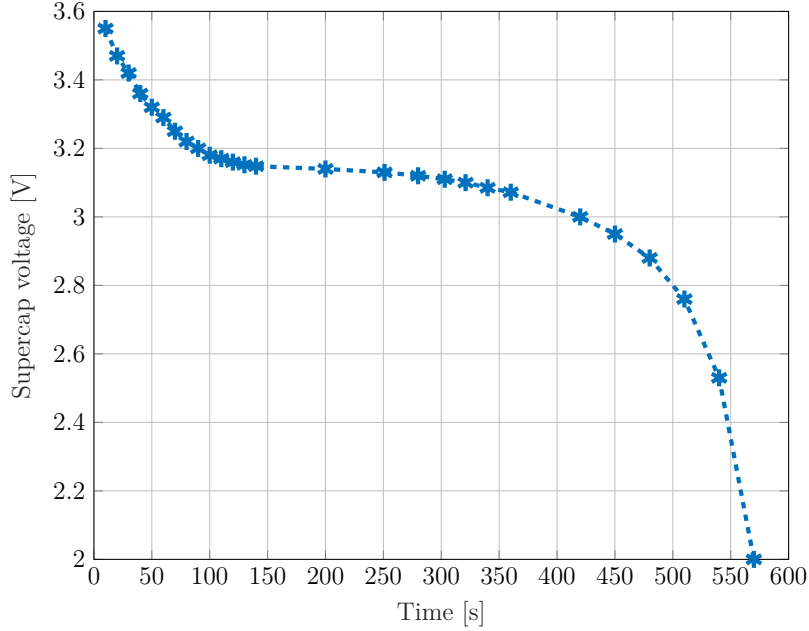


Figure 8.3: Supercapacitor discharge under a constant current of 500 mA

Sound analysis

Pure sine wave

To validate the sensing subsystem, a first test is achieved with a pure sine wave at 1 kHz generated from a laptop speaker. Figure 8.4 presents the results in the time and frequency domains. This sound is fully detected by the microcontroller, with a sharp peak at 1 kHz in the spectral domain. The voltage decrease is probably due to the ADC discharging the node by drawing some current when it samples the signal.

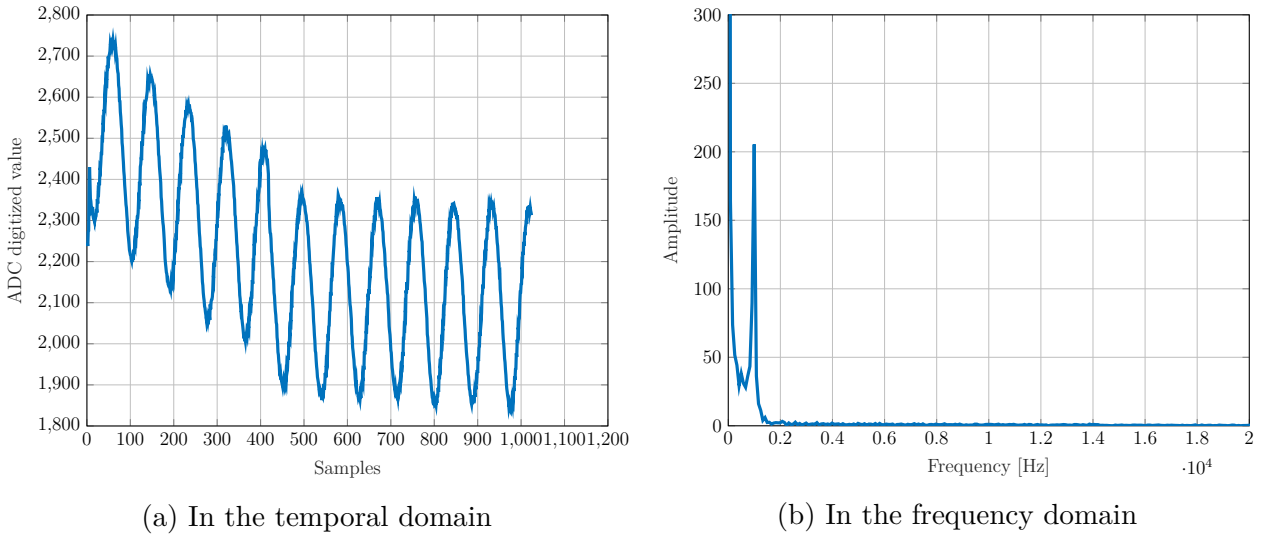


Figure 8.4: Analysis of a pure sine wave at 1 kHz

Noise

Figure 8.5 shows a digitized signal under a quiet environment in order to determine the intrinsic noise of the sensing system. The RMS noise value, in terms of LSBs, is given by

$$E_{\text{RMS}} = \sqrt{\frac{1}{N} \sum_n (x[n] - E[x])^2} = 23.6 \text{ LSBs}$$

where N is the number of samples, $x[n]$ is the n -th ADC digitized value and $E[x]$ is the mean of x . This value can be compared to the theoretical value, $E_{\text{RMS}} = 18.7 \text{ LSBs}$ since $V_{\text{N,tot,theor}} = 11.2 \text{ mV}$ and one LSB is $V_{\text{CC}}/2^{12} = 0.6 \text{ mV}$. The excess noise is due to the environmental noise that remains at the microphone input, which is always present except in an anechoic chamber.

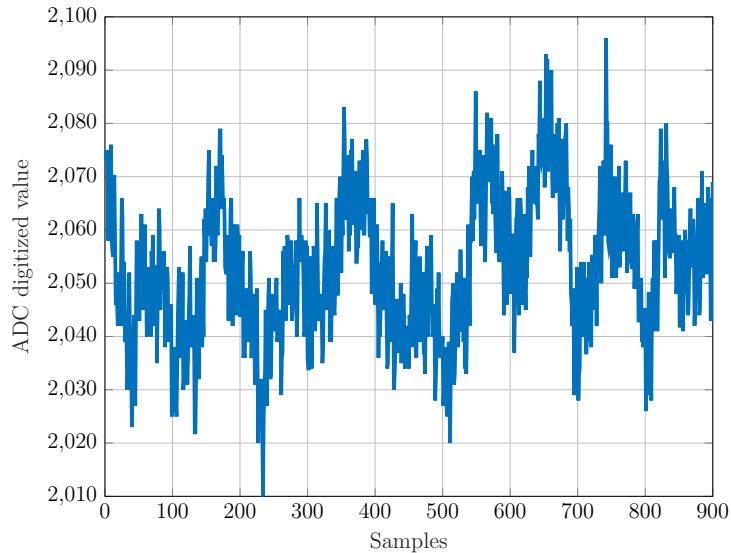


Figure 8.5: Noise at the ADC input

Requirements review

Finally, one will review the requirements stated at the beginning of this work (see Section 2.3). The requirements related to bird classification will be discussed in the next chapter.

Lifetime

The lifetime is limited by the supercapacitor, which is expected to work about 11 200 h at 60 °C according to the datasheet [23]. The 10-degrees-rule for electrolytic capacitors can be used to estimate supercapacitor lifetimes. This rule employs the Arrhenius equation, and states that for every 10 °C reduction in operating temperature, the estimated life doubles. The expected lifetime L at 20 °C is thus given by

$$L = L_0 2^{\frac{T_0-T}{10^\circ\text{C}}} = 179\,200 \text{ h}$$

which corresponds to 20.5 years. It can even be increased above 20 years with additional equalization methods [45]. As required, the sensor is working fully autonomously (day and night) for more than 15 years.

Volume and cost

One first confirms that the total volume is inside the constraint (200 mm × 200 mm × 50 mm): 143 mm × 82 mm × 25 mm.

The overall cost, including the PCB, is 74.28 euros. The most important costs are the solar cells (30.4 euros), the supercapacitor (17.5 euros) and the PCB (20 euros). In order to stay below the limit of 15 euros, both the solar cells and supercap need to have a smaller size by reducing the power consumption. Indeed, typical ultra-low-power sensors have a power consumption in the order of the μW [21]. This constraint implies further concessions on the audio processing period over a day. Particularly when the reduced solar cells are strongly limited by the sun illuminance (i.e. in winter), one has to allow the sensor to have a shorter processing period (which fortunately has not much impact since birds are less active in this season). In a massive development, buying in bulk will further help decrease overall costs.

Sound detection

Determining the detection distance is probably the most difficult requirement to precisely characterize. It can be based on real-time songs but birds are singing intermittently and with different sound amplitudes. It can also be characterized by a speaker emitting bird songs, but the sound pressure cannot either be known without a sound level meter. Still, the device has been able to detect pure sine waves with speakers at reasonable distance, as well as bird songs as depicted in the next chapter.

Chapter 9

Inference algorithm

This chapter will present different algorithms aiming to discriminate bird species based on the microphone signal. This temporal signal is often transformed into its dual domain: the spectral (or frequency) domain. Representing a signal in the spectral domain is done through the Fourier transform, which is in fact a fast Fourier transform (FFT) for digitized data (such as data stored in a microcontroller).

The requirements in Section 2.3 state that the sensor has to discriminate among four very common birds in Belgian forests. These species are the pigeon, blackbird, great tit, and blue tit. The remaining of the section will demonstrate the ability of the sensor node to find the correct species with sufficient precision.

9.1 Peak frequency extraction

The first algorithm will process bird songs based on the frequency at which the signal has the most power. Because the FFT size is limited by computation time, it is not possible to record and process sound over an entire bird song duration (typically 2 s). On the other hand, one cannot decrease the sampling frequency below 20 kHz in order to detect useful frequencies below 10 kHz¹, which would give 40 000 samples during a typical song duration. It is thus required to spread the sampling duration over multiple time windows. For example, Figure 9.1 shows the peak frequency² for each time window (32 ms whose 6.4 ms to retrieve 128 samples at 20 kHz) of a great tit song. One can roughly see two sounds spaced by 4 ms and oscillating between 3 kHz and 4.5 kHz. Based on the graph, it is thus possible to discriminate visually between species with substantially different frequency profiles, but formalizing further embedded processing to extract meaningful information from this peak frequency graph is less trivial.

Although this algorithm shows good visual results, this kind of algorithm misses important information for different reasons.

First, most bird songs present several high amplitudes for different frequencies at the same time, these secondary frequencies are never detected. This means that several bird songs with the

¹The Nyquist–Shannon sampling theorem states that, to avoid loss of information during a sampling process, a sampling frequency larger than twice the maximum frequency contained in the signal is required.

²That is, there is only one frequency associated with each time sample.

same peak frequency but different secondary frequencies are never discriminated.

Second, several birds present different frequency profiles during their song, that is to say the FFT is varying with time (e.g. 3 kHz and 4.5 kHz for the song presented in Figure 9.1). Thereby, characterizing birds based on one FFT over a short period of time misses non-harmonious (or non-periodic) bird songs and cannot discriminate two birds with the same frequency peak in the beginning of their song, for example.

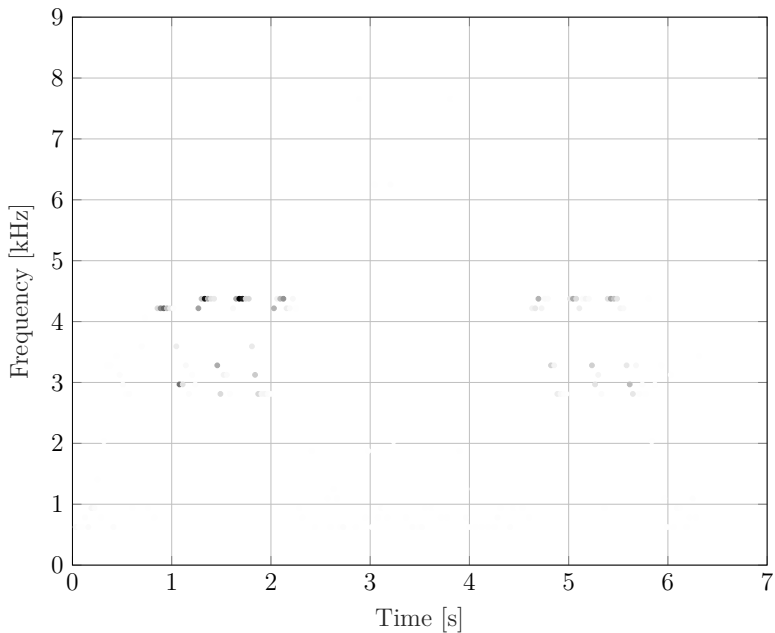


Figure 9.1: Peak frequencies associated with a great tit song

9.2 Spectrogram decomposition

From the previous remarks, it is more convenient to represent the signal with a spectrogram: the visual representation of the spectrum of frequencies of a signal as it varies with time. Creating a spectrogram using the FFT is a digital process. Digitally sampled data, in the time domain, are broken up into chunks, which usually overlap, and Fourier transformed to calculate the magnitude of the frequency spectrum for each chunk. Each chunk then corresponds to a vertical line in the image, which provides the magnitude versus frequency for a specific moment.

A smaller (shorter) window will produce more accurate results in timing, at the expense of precision of frequency representation. This leads to the consideration of trade-offs between time and frequency resolution in audition: the bandwidth can only be narrowed (i.e. the frequency resolution increased) if the temporal resolution is decreased, because narrower filters have longer time constants. In the design of linear filters, the uncertainty principle fixes a limit on the resolution that can be attained (the Gabor limit³), giving a lower bound for the product of the variance in time and the variance in frequency for a single linear filter [46].

³It is nothing else than the Heisenberg's uncertainty principle applied in the context of signal processing to time and frequency (2 dual physical quantities).

Some birds have several typical songs. For example, Figure 9.2 presents the spectrogram for two common songs of the blue tit. As human perception of sound intensity is logarithmic [47], the graphs are given in the form of log scale.

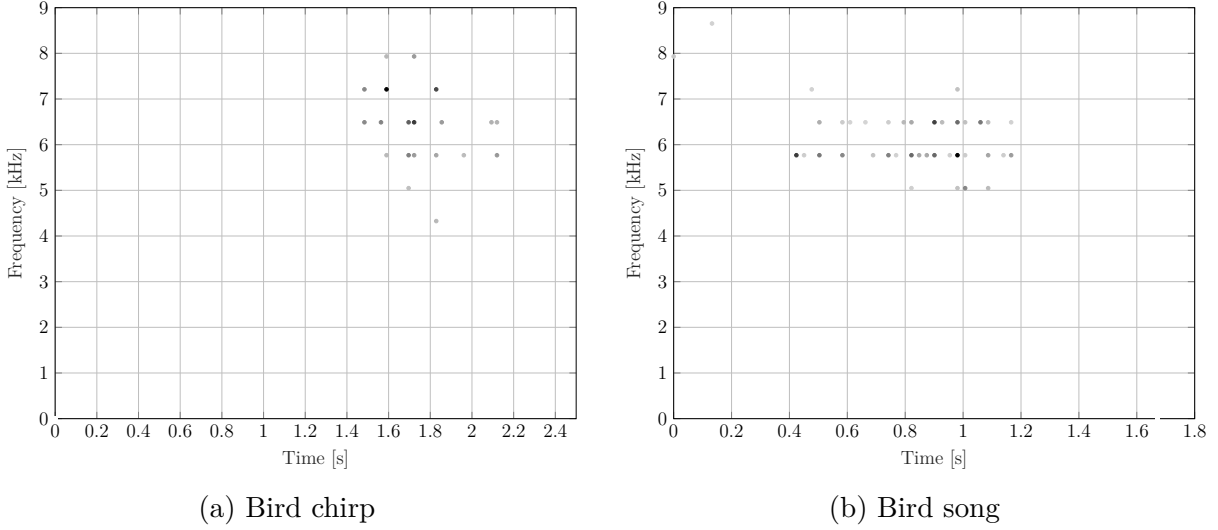


Figure 9.2: Spectrograms of two sounds from the blue tit computed with this sensor node

Due to the limited memory, the signal has to be processed at each time window. This considerably increases the delay between adjacent time windows, given by 26.5 ms for an FFT size of $N = 128$ (see Table 9.1).

Time [ms]	
Data sampling	1.28
FFT	25
Data storage	0.2
Total	26.5

Table 9.1: Processing time for one spectrogram data chunk with 128 samples

In this case, the sampling period is set to 10 μ s, corresponding to a sampling frequency $f_s = 100$ kHz. Hence, the frequency resolution in the spectrogram is given by

$$\Delta f = \frac{f_s}{N} = 781 \text{ Hz}$$

with a maximum analyzed frequency of $f_s/2 = 50$ kHz. One can finally see the trade-off appearing on the frequency resolution, which cannot be improved (that is, decreased) without

- increasing N , which would require more memory storage and processing time (the FFT time evolving according to $\mathcal{O}(N^2)$, or $\mathcal{O}(N \log N)$ with optimized algorithms [48]),
- or decreasing f_s , which would increase the sampling time (impinging on the time window length).

Figure 9.3 provides the time–frequency comparison of four different bird songs. As discussed, the frequency resolution is also 781 Hz. This makes discrimination among the birds very difficult since some peak frequencies are identical for several birds.

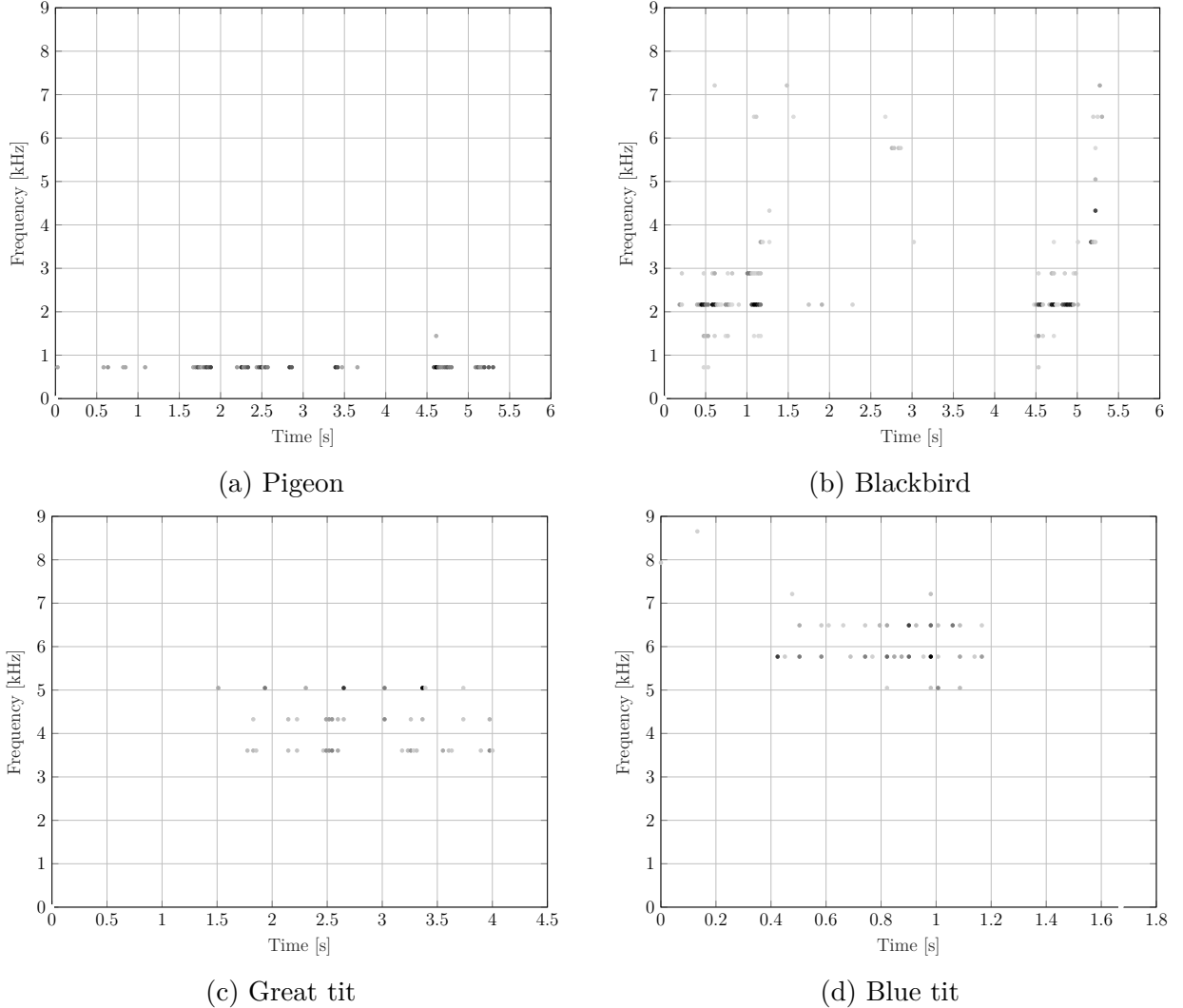


Figure 9.3: Spectrograms of four different bird songs computed with this sensor node

To illustrate the difference, Figure 9.4 shows the spectrogram of the great tit when the signal does not significantly suffer from the time–frequency trade-off (that is, the graph has been computed in offline mode from an audio file at 44.1 kHz). One can clearly see four songs oscillating between 3 kHz and 6 kHz, which is not detected by the embedded low-resource microcontroller (see Figure 9.3c). It will thus be needed to work on specific characteristics of the signal instead of the whole spectrogram pattern.

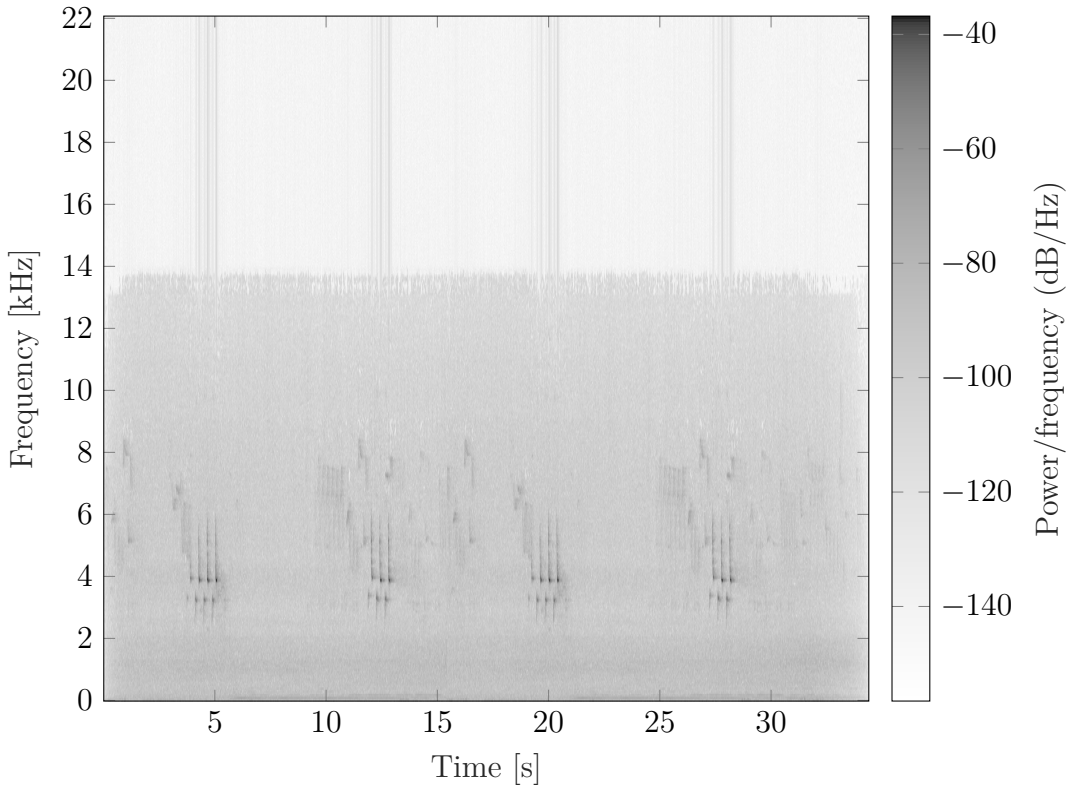


Figure 9.4: Precise spectrogram of the great tit song (from a bird song database)

Feature extraction

Now that the signal has been converted into meaningful information via its spectrogram form, some features need to be extracted from it. Typical features for bird recognition are specific frequencies for each time window, the median as well as the 5 and 95 percentiles which are robust measures of minimum and maximum frequency [46]. The bandwidth can also be extracted, defined as the difference between the 5 and 95 percentiles.

For this work, the average frequency weighted by the intensity is analyzed because of its simplicity and robustness. In a spectrogram, let $f[i]$ be the vector of discrete frequencies (y -axis) with size $N/2$, $t[j]$ be the vector of discrete time samples (x -axis) with size M (depending on the audio recording time and the window overlap) and $s[i, j]$ be the intensity of the i -th frequency component during the j -th time period, then the average intensity for the i -th frequency component throughout the time period is

$$s_{\text{avg}}[i] = \frac{1}{M} \sum_{j=1}^M s[i, j] \quad [\text{dB/Hz}]$$

and the weighted average frequency is given by

$$f_{\text{avg}} = \frac{\sum_{j=1}^L s_{\text{avg}}[i] f[i]}{\sum_{j=1}^L s_{\text{avg}}[i]} \quad [\text{Hz}]$$

where L is the index corresponding to a frequency of 10 kHz in order to remove high-frequency noise from the average. The spectrogram has frequencies above this range if $f_{\text{max}} > 10 \text{ kHz}$,

that is $f_s > 20$ kHz. The sampling frequency is thus fixed to $f_s = 20$ kHz in order to remove significant noise while keeping the useful bandwidth of bird song (below 10 kHz).

During calibration, the mean background noise (expressed as power spectral density) is characterized for each frequency, resulting in a combination of $1/f$ and white noise. It is then removed from the intensity $s[i, j]$ when a real signal is analyzed. The algorithm is also tuned by an intensity threshold to output a bird species only when the signal sufficiently exceeds the background noise, meaning that a sound has been produced.

Feature selection

Additionally, feature selection is used to evaluate the predictive power that a feature has with respect to some attribute. In information gain feature selection, each feature is evaluated by measuring the information gain with respect to the species label, which is the amount by which the feature reduces the uncertainty in the label. To reduce the problem complexity, the weighted average frequency is kept in this work. The problem thus becomes a 1D classification.

Inference

The final step consists to infer the species based on the selected feature. A simple machine-learning model for this purpose is the support vector machine (SVM), but it requires much offline preprocessing beforehand. Since only one feature is analyzed, a complex machine-learning algorithm has little interest. The classifier used for this work is based on a k -nearest neighbors algorithm (KNN) with $k = 5$, meaning that the class (i.e. the species) associated with a new sample is classified by a plurality vote among the k nearest data according to the feature (i.e. the weighted average frequency).

A learning phase now consists to analyze several songs from the six species previously mentioned, and extract the weighted average frequency for all these learning samples. Figure 9.5 shows the repartition of the weighted average frequency among the species learning samples, based on the spectrogram of six different audio samples for each species⁴.

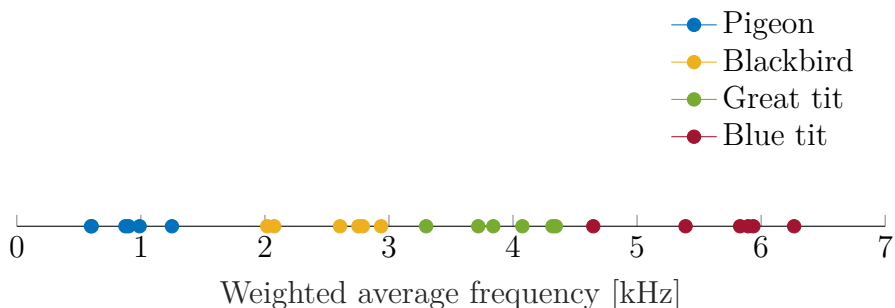


Figure 9.5: Repartition of the weighted average frequency among the species learning samples

One can deduce that the weighted average frequency is actually a pertinent feature with useful information since it discriminates quite well between the different species.

⁴The audio files come from a collaborative and open-source database of bird songs (*xeno-canto* [49]).

Then, these frequencies are stored inside the sensor node in order to infer the species of a newly recorded song. The microcontroller launches a KNN classifier by selecting the species which is the most similar to the new sample (that is, which has the nearest weighted average frequency).

Experimental results

To validate the theoretical work, bird songs are generated from a laptop speaker in the area around the sensor node. Based on the KNN algorithm and these thresholds encoded in the microcontroller, Table 9.2 provides the number of right predictions on the learning samples with the very-low-precision algorithm inside the microcontroller. Surprisingly, it manages to retrieve the correct species with more than 94% of precision on average.

Species	Number of correct predictions
Pigeon	6/6
Blackbird	6/6
Great tit	6/6
Blue tit	4/6

Table 9.2: Number of right predictions on the learning samples with the sensor node

It is now possible to test the algorithm on new samples, which can either be additional audio files in a database or real-time songs from birds in the vicinity. One will focus on the former since real-time songs are too sporadic to be precisely characterized. For each species, positions of three testing samples are given in Figure 9.6. One can see that the KNN algorithm is able to find the correct for all new samples.

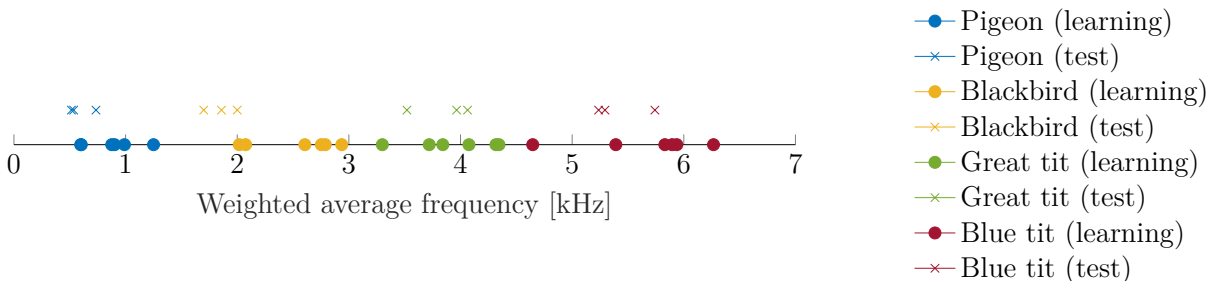


Figure 9.6: Predictions on new samples with the sensor node

Chapter 10

Improvement perspectives

Some improvements could be made to further refine the main objectives of this smart sensor.

10.1 Power management

As discussed before, one could first decrease the power consumption and hence the size of the device at the cost of less precise and frequent audio monitoring. This solution has not been considered in this work due to the strong expectations imposed at the beginning to monitor with precision the forest. This possibility should however be carefully reviewed for every person willing a massive and cheap deployment of such sensors by this time.

Second, the power management unit from e-peas is excessively successful in terms of power losses reduction, but it limits the storage element voltage at 4.5 V. By increasing this voltage limitation to 5.5 V and beyond, the supercapacitor could store much more useful energy. If this limitation is increased to 6.3 V, aluminum electrolytic capacitors could be used with an even smaller capacitance size. This technology has an advantage in terms of lifetime compared to other supercapacitor technologies. Still, one should keep in mind that this voltage increase is meaningless without a change of the internal DC-DC converter from the storage element to the supply voltage, which has to be a buck converter (that is, with high efficiency whatever the input voltage) in place of the low-dropout regulator currently used in the AEM10941 (whose efficiency drops below 50 % when the input voltage is twice the supply voltage: 5 V).

10.2 Refinement of inference algorithms

The majority of discrimination algorithms are done thanks to machine-learning algorithms applied on the time-frequency texture. Typical models use convolutional neural networks (CNNs) and/or recurrent neural networks (RNNs). With deep learning, bird detection can achieve very high retrieval rates in remote monitoring data, with no manual recalibration, and no pretraining of the detector for the target species or the acoustic conditions in the target environment [50].

Other less resource-intensive models use feature extraction performed by matching the time-frequency plane with a number of time-frequency blocks previously learned. The minimum

matching energy of the blocks makes a feature vector of the audio signal and is sent to a classifier for song discrimination [51]. However, these models require a substantial amount of memory and speed, which is impractical for embedded applications. Still, one could optimize these memory/time/energy trade-offs based on the microcontroller capabilities in order to extract meaningful information.

Additionally, the present algorithm is not able to find other species. It will thus output one of the four species even for other species and external sounds (such as traffic noise), creating so-called false positive detections. The algorithms previously mentioned would greatly help solve this issue.

10.3 Robustness under difficult conditions

The device can be further designed to integrate a robust protection against difficult environmental conditions. One can for example cite a waterproof case which supports high temperature variations. Potting the entire PCB would also help reduce oxidation and support shocks/vibration which are paramount for an expected lifetime exceeding 15 years.

Chapter 11

Conclusion

The Internet of Things (IoT) is predicted to lead to the deployment of a very large number of connected smart sensors for various applications, which is not environmentally sustainable if the devices are frequently replaced. Additionally, rising climate change due to ecosystem destruction demands to automatically monitor forests in order to analyze and preserve the ecosystem.

In this master thesis, the focus is on the development of an autonomous and efficient audio smart sensor continuously analyzing the forest ecosystem. To fulfill the energy constraints implied by its total autonomy, this sensor harvests energy from the environment through miniaturized photovoltaic cells sized according to the sun illuminance throughout days and seasons, using an environmentally-friendly and non-toxic supercapacitor to store energy. With a 15+ year lifetime, this fully autonomous device operates at an optimized 2.5 V supply voltage reaching 22.1 mW of average power harvesting/consumption. An electret condenser microphone collects a signal as low as 16 dB_{SPL} (compared to a 14.22 dB_{SPL} input-referred noise), which is then amplified in the full frequency range of bird emission (20 Hz – 20 kHz) by a low-noise and low-power analog front-end. This signal is further processed in an ultra-low-power chip embedding a microcontroller, alternating between run and sleep modes with a 1/3 duty cycle, and a transceiver optimized for IoT applications with LoRaWAN networks.

The microcontroller detects sounds when birds are active (typically during the day for more than 12 hours) and ensures the radio-frequency communication at night depending on the supercapacitor voltage that is carefully monitored in real time. It sends information about the bird species encountered during the day, as well as their apparition frequency. In case of firmware update, this device receives the associated fragments when its energy is sufficient and it automatically changes the firmware with energy-optimized software requiring only 10.6 J for the whole update.

By computing the weighted average frequency of the received sounds, the smart sensor is able to discriminate between four common birds in Belgium: the pigeon, blackbird, great tit and blue tit. For each species, several songs have been analyzed and used to train a k -nearest neighbors (KNN) classifier working in the real-time embedded system. Its precision, defined as the likelihood to find the correct species, reaches 94% for songs coming from the previously learned database. For newly analyzed sounds, the detection algorithm performs likewise. More complex machine-learning algorithms could finally be further designed to discriminate between

more species.

SWOT analysis

A SWOT analysis is a strategic technique used to help identify strengths, weaknesses, opportunities, and threats related to a concept [52]. Depicted in Table 11.1, it concludes this work by summarizing the principal characteristics of the smart sensor, which have all been well detailed in Chapters 10 and 11.

	<i>Positive</i>	<i>Negative</i>
<i>Internal</i>	Strengths: <ul style="list-style-type: none">• Fully autonomous and low power• Long lifetime (15+ years)• Environmentally-friendly• Bird classification	Weaknesses: <ul style="list-style-type: none">• Resource-limited inference algorithm• Size of the sensor node• Production cost
<i>External</i>	Opportunities: <ul style="list-style-type: none">• High demand for sustainable sensors and forest monitoring• Rising of low-power machine-learning algorithms	Threats: <ul style="list-style-type: none">• Harsh environmental conditions

Table 11.1: SWOT analysis of this smart sensor

Appendix A

Transimpedance amplifier

Figure A.1 presents the transimpedance amplification circuit simplified in the audio frequency.

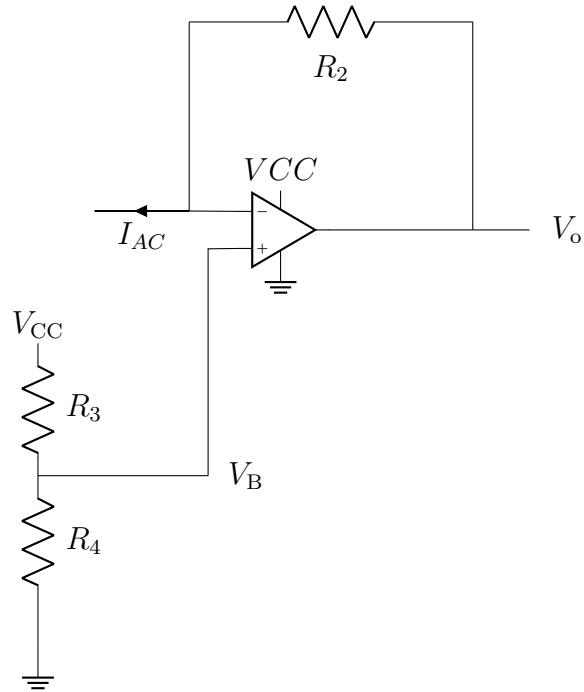


Figure A.1: Simplified transimpedance amplification circuit

The voltage at the negative terminal of the op-amp is given by

$$V_- = V_o - R_2 I_{AC} \quad [\text{V}].$$

Since the positive and negative terminals of an op-amp are identical (ideally), the relation becomes

$$V_B = V_o - R_2 I_{AC} \quad \Rightarrow \quad V_o = V_B + R_2 I_{AC} \quad [\text{V}],$$

which is the transimpedance transfer function of the circuit.

Appendix B

Noise gain of the microphone amplifier

Figure B.1 presents the transimpedance amplification circuit simplified in the audio frequency. The supply voltage (DC) is grounded and the microphone (input current source) is open-circuited. Noise gain is referred to the noise source, which is connected to the noninverting input by definition.

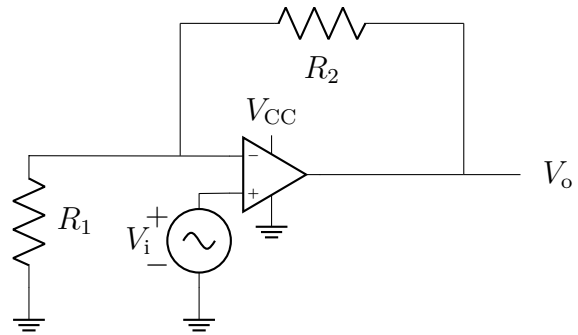


Figure B.1: Simplified transimpedance amplification circuit for the noise gain

The voltage at the negative terminal of the op-amp is given by

$$V_- = \frac{R_1}{R_1 + R_2} V_o \quad [\text{V}].$$

Since the positive and negative terminals of an op-amp are identical (ideally), the relation becomes

$$\frac{V_o}{V_i} = 1 + \frac{R_2}{R_1} \quad [\text{V}],$$

which is the noise gain of the circuit.

Appendix C

PCB layout and schematic

The PCB layout (see Figure C.1) and schematic (see Figure C.2) were designed with KiCad. The PCB is composed of four layers, of which two are for GND and VDD.

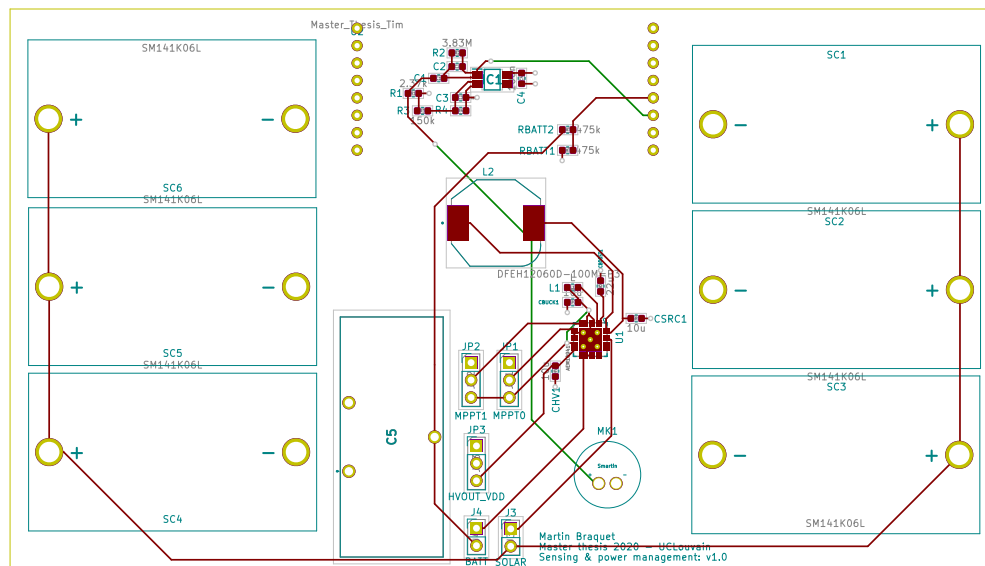


Figure C.1: PCB layout

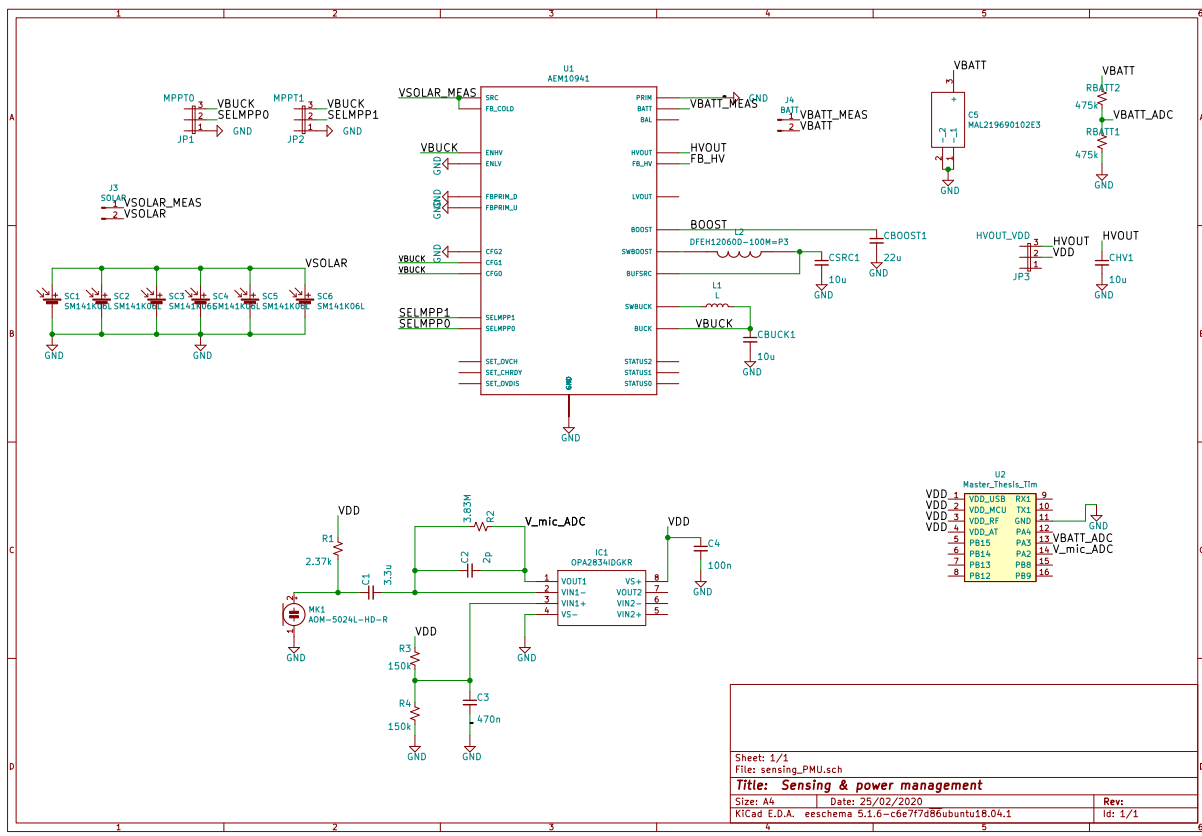


Figure C.2: PCB schematics

Bibliography

- [1] K. Meyer-Schulz and R. Bürger-Arndt. Les effets de la forêt sur la santé physique et mentale. une revue de la littérature scientifique. *Revue Forestière Française*, page 243, 01 2018.
- [2] M. Fauzi Othman and K. Shazali. Wireless sensor network applications: A study in environment monitoring system. *Procedia Engineering*, 41:1204 – 1210, 2012. International Symposium on Robotics and Intelligent Sensors 2012 (IRIS 2012).
- [3] A. Michel, A.-K. Prescher, W. Seidling, and M. Ferretti. ICP Forests Brief No 1 - ICP Forests: A policy-relevant infrastructure for long-term, large-scale assessment and monitoring of forest ecosystems. 05 2018.
- [4] I. Akyildiz, W. Su, Y. Sankarasubramaniam, and E. Cayirci. A survey on sensor networks. *Communications Magazine, IEEE*, 40:102 – 114, 09 2002.
- [5] C. Pérez G., G. Bota, D. Giralt, A. Diego, J. Gómez Catasús, D. Bustillo de la Rosa, and J. Traba. Vocal activity rate index: a useful method to infer terrestrial bird abundance with acoustic monitoring. *Ibis*, 161:901–907, 03 2019.
- [6] H. Tao and H. Zhang. Forest monitoring application systems based on wireless sensor networks. *2009 Third International Symposium on Intelligent Information Technology Application Workshops*, 0:227–230, 11 2009.
- [7] X. Jiang, G. Zhou, Y. Liu, and Y. Wang. Wireless sensor networks for forest environmental monitoring. pages 2514–2517, 12 2010.
- [8] D. Bol, M. Schramme, L. Moreau, T. Haine, P. Xu, C. Frenkel, R. Dekimpe, F. Stas, and D. Flandre. A 40-to-80MHz Sub-4 μ W/MHz ULV Cortex-M0 MCU SoC in 28nm FDSOI With Dual-Loop Adaptive Back-Bias Generator for 20 μ s Wake-Up From Deep Fully Retentive Sleep Mode. In *2019 IEEE International Solid-State Circuits Conference - (ISSCC)*, pages 322–324, 2019.
- [9] M. Cerchecci, F. Luti, A. Mecocci, S. Parrino, G. Peruzzi, and A. Pozzebon. A low power IoT sensor node architecture for waste management within smart cities context. *Sensors*, 18:1282, 04 2018.
- [10] D. Bol. Ultra-Low-Power SoCs for Local Sensor Data Processing. *Forum presentation at the IEEE International Solid-State Circuits Conference*, 02 2018.
- [11] D. Bol. Ultra-low-power wireless communications for IoT smart sensors. *ESSCIRC*, 2018.

- [12] W. Shi, J. Cao, Q. Zhang, Y. Li, and L. Xu. Edge computing: Vision and challenges. *IEEE Internet of Things Journal*, 3:1–1, 10 2016.
- [13] E. Vincent, R. Gribonval, and C. Févotte. Performance measurement in blind audio source separation. *Audio, Speech, and Language Processing, IEEE Transactions on*, 14:1462 – 1469, 08 2006.
- [14] R. F. Service. New 'supercapacitor' promises to pack more electrical punch. *Science*, 313(5789):902–902, 2006.
- [15] J. F. M. Oudenhoven, R. J. M. Vullers, and R. van Schaijk. A review of the present situation and future developments of micro-batteries for wireless autonomous sensor systems. *International Journal of Energy Research*, 36:1139–1150, 2012.
- [16] J. Monteiro Baptista, J. S. Sagu, U. Wijayantha KG, and K. Lobato. State-of-the-art materials for high power and high energy supercapacitors: Performance metrics and obstacles for the transition from lab to industrial scale – a critical approach. *Chemical Engineering Journal*, 374:1153 – 1179, 2019.
- [17] P. R. Bueno. Nanoscale origins of super-capacitance phenomena. *Journal of Power Sources*, 414:420–434, February 2019.
- [18] H. Sun, J. Zhu, D. Baumann, L. Peng, Y. Xu, I. Shakir, Y. Huang, and X. Duan. Hierarchical 3d electrodes for electrochemical energy storage. *Nature Reviews Materials*, 4(1):45–60, 2019.
- [19] W. Liu, Z. Chen, G. Zhou, Y. Sun, H. Lee, C. Liu, H. Yao, Z. Bao, and Y. Cui. 3d porous sponge-inspired electrode for stretchable lithium-ion batteries. *Advanced Materials*, 28(18):3578–3583, 2016.
- [20] Y. Chen, Z. Wang, X. Li, X. Yao, C. Wang, Y. Li, W. Xue, D. Yu, S. Y. Kim, F. Yang, A. Kushima, G. Zhang, H. Huang, N. Wu, Y.-W Mai, J. Goodenough, and J. Li. Li metal deposition and stripping in a solid-state battery via coble creep. *Nature*, 2020.
- [21] R. Dekimpe, P. Xu, M. Schramme, P. Gérard, D. Flandre, and D. Bol. A battery-less BLE smart sensor for room occupancy tracking supplied by 2.45-GHz wireless power transfer. *Integration*, 67:8 – 18, 2019.
- [22] Murata. DMF3Z5R5H474M3DTA0: 470mF (EDLC) Supercapacitor 5.5V. 2017.
- [23] Vishay BCcomponents. Hybrid energy storage capacitors. 2019.
- [24] C. Yuan, Y. Deng, T. Li, and F. Yang. Manufacturing energy analysis of lithium ion battery pack for electric vehicles. *CIRP Annals - Manufacturing Technology*, 66, 05 2017.
- [25] R. Hastak, P. Sivaraman, D. Potphode, S. Kannakaje, and A. Samui. High temperature all solid state supercapacitor based on multi-walled carbon nanotubes and poly[2,5 benzimidazole]. *Journal of Solid State Electrochemistry*, 16, 10 2012.
- [26] e-peas. AEM10941: Highly-efficient, regulated dual-output, ambient energy manager for up to 7-cell solar panels with optional primary battery, 2018.
- [27] J. Ahmad. A fractional open circuit voltage based maximum power point tracker for

- photovoltaic arrays. *2nd International Conference on Software Technology and Engineering*, 2010.
- [28] Federal Highway Administration. Noise effect on wildlife, 2017. Online; accessed 26 December 2019.
 - [29] A. Mack and J. Josh. Low-frequency vocalizations by cassowaries (*casuarius spp.*). *The Auk*, 120(4):1062–1068, 2003.
 - [30] W. H. Thorpe and D. R. Griffin. Ultrasonic frequencies in bird song. *Ibis*, 104(2):220–227, 1962.
 - [31] S. Oksanen and V. Valimaki. Modeling of the carbon microphone nonlinearity for a vintage telephone sound effect. *14th International Conference on Digital Audio Effects*, pages 27–30, 2011.
 - [32] C. Garcia. Packaging and characterization of MEMS optical microphones. page 44, 2019.
 - [33] InvenSense. ICS-40720: Ultra-low noise microphone with differential output, 2016. Rev. 1.3.
 - [34] P. Malcovati and A. Baschirotto. The evolution of integrated interfaces for MEMS microphones. *Micromachines*, 9:323, 2018.
 - [35] PUI Audio. PMM-3738-VM1000-R: Low-noise bottom port piezoelectric MEMS microphone, 2017.
 - [36] J. Caldwell. Single-supply, electret microphone pre-amplifier reference design. *TI Designs*, 2015.
 - [37] H. Brumm. Song amplitude and body size in birds. *Behav Ecol Sociobiol*, 2009.
 - [38] STMicroelectronics. STM32L072xx: Ultra-low-power 32-bit MCU Arm-based Cortex-M0+, up to 192KB Flash, 20KB SRAM, 6KB EEPROM, USB, ADC, DACs, 2019.
 - [39] Semtech. SX1276/77/78/79 - 137 MHz to 1020 MHz Low Power Long Range Transceiver, 2019.
 - [40] R. Sharan Sinha, Y. Wei, and S.-H. Hwang. A survey on LPWA technology: LoRa and NB-IoT. *ICT Express*, 3(1):14 – 21, 2017.
 - [41] T. Hess. Ultra-low-power over-the-air-update in secure LoRaWAN networks. *Ecole polytechnique de Louvain, Université catholique de Louvain*, 2020.
 - [42] World Data. <https://www.worlddata.info/europe/belgium/sunset.php>, Online; accessed 25 March 2020.
 - [43] S.A. Ackerman and J.A. Knox. *Meteorology: Understanding the Atmosphere*. Available Titles CengageNOW Series. Thomson Brooks/Cole, 2007.
 - [44] Keithley. 2400 series sourcemeter: User's manual. 1998.
 - [45] F. I. Simjee and P. H. Chou. Efficient charging of supercapacitors for extended lifetime of wireless sensor nodes. *IEEE Transactions on Power Electronics*, 23(3):1526–1536, May 2008.

- [46] D. Stowell and M. Plumbley. Large-scale analysis of frequency modulation in birdsong databases. *Methods in Ecology and Evolution*, 5:901–912, 09 2014.
- [47] H. Fastl and E. Zwicker. Psychoacoustics: Facts and models. *Springer-Verlag Berlin Heidelberg*, 2007.
- [48] S. Qiu, F. Zhou, and P. E. Crandall. Discrete gabor transforms with complexity $O(n\log n)$. *Signal Processing*, 77(2):159 – 170, 1999.
- [49] xeno-canto: sharing bird sounds from around the world. <https://www.xeno-canto.org>, Online; accessed 30 May 2020.
- [50] D. Stowell, M. Wood, H. Pamuła, Y. Stylianou, and H. Glotin. Automatic acoustic detection of birds through deep learning: The first bird audio detection challenge. *Methods in Ecology and Evolution*, 10, 10 2018.
- [51] G. Yu and J. Slotine. Audio classification from time-frequency texture. In *2009 IEEE International Conference on Acoustics, Speech and Signal Processing*, pages 1677–1680, April 2009.
- [52] T. Hill and R. Westbrook. SWOT analysis: It’s time for a product recall. *Long Range Planning*, 30(1):46 – 52, 1997.

UNIVERSITÉ CATHOLIQUE DE LOUVAIN
École polytechnique de Louvain
Rue Archimède, 1 bte L6.11.01, 1348 Louvain-la-Neuve, Belgique | www.uclouvain.be/epl